

Stability of quantized vortices in two-component condensates

Sam Patrick^{1,*}, Ansh Gupta^{1,†}, Ruth Gregory^{1,2,‡} and Carlo F. Barenghi^{3,§}

¹*Department of Physics, King's College London, The Strand, London WC2R 2LS, United Kingdom*

²*Perimeter Institute, 31 Caroline Street, Waterloo, Ontario, Canada N2L 2Y5*

³*Joint Quantum Centre Durham-Newcastle, School of Mathematics, Statistics and Physics, Newcastle University, Newcastle upon Tyne NE1 7RU, United Kingdom*



(Received 9 May 2023; accepted 9 August 2023; published 20 September 2023)

Multiply quantized vortices (MQVs) within single-component Bose-Einstein condensates are unstable and decay rapidly. We show that MQVs can be stabilized by adding a small number of atoms of a second species to the vortex cores, and that these atoms remain in the vortex core as the system evolves. A consequence of the stabilization is that nearby corotating vortices can orbit in the opposite sense to their individual rotations when enough of the second species is present. This has implications concerning the imaging of vortices, as well as quantum turbulence and vortex nucleation in two-component condensates, such as those involving mixtures of ⁸⁷Rb and ¹³³Cs.

DOI: [10.1103/PhysRevResearch.5.033201](https://doi.org/10.1103/PhysRevResearch.5.033201)

I. INTRODUCTION

The most striking property of quantum fluids (superfluid ⁴He, atomic Bose-Einstein condensates, polariton condensates, etc.) is the existence of a macroscopic complex wave function $\Psi(\mathbf{x}, t)$, where \mathbf{x} is the position and t is time. If we write the wave function as $\Psi = |\Psi|e^{i\Phi}$ in terms of its amplitude $|\Psi|$ and phase Φ , then the density n and the velocity \mathbf{v} of the superfluid are [1]

$$n(\mathbf{x}, t) = |\Psi(\mathbf{x}, t)|^2, \quad \mathbf{v}(\mathbf{x}, t) = \frac{\hbar}{M} \nabla \Phi(\mathbf{x}, t), \quad (1)$$

where \hbar is the reduced Planck's constant and M is the mass of the relevant boson. The wave function imposes constraints on the rotational motion. Whereas rotation in ordinary (classical) fluids takes the form of eddies of arbitrary size and circulation, rotation in superfluids is quantized, occurring around special points (in two dimensions) or lines (in three dimensions) called quantized vortices. At these special points, the density n is exactly zero, hence the phase Φ is not defined: Quantized vortices are therefore phase defects. Within a superfluid, the circulation Γ of the velocity along a closed path C is either zero if the region inside C does not include any vortex, or an integer multiple ℓ of the quantum of circulation $\kappa = 2\pi\hbar/M$ [1],

$$\Gamma = \oint_C \mathbf{v} \cdot d\mathbf{r} = \ell\kappa, \quad (2)$$

if the region inside C includes a vortex of quantization ℓ (since Ψ must be continuous, ℓ must take on integer values). This condition strongly constrains the velocity field around the vortex axis. Vortices with $|\ell| = 1$ are commonly referred to as singly quantized vortices (SQVs), whereas $|\ell| > 1$ are called multiply quantized vortices (MQVs) (ℓ is commonly called the “charge” of the vortex). Since the angular momentum and the kinetic energy carried by a vortex are proportional to ℓ and ℓ^2 , respectively, MQVs are energetically unstable [2–4] in simple homogeneous superfluids [5]; any MQV with charge ℓ will rapidly decay into ℓ SQVs carrying the same total angular momentum. This decay is the result of an energetic instability in the spectrum of the vortex, i.e., the vortex possesses a normal mode with negative energy. In the presence of a dissipation mechanism, the amplitude of this mode will grow eventually causing the central vortex to split up. In large enough systems, the surrounding bath of sound waves can also act as a reservoir for the vortex to dissipate energy into, allowing MQVs to split even when the governing equations are energy-conserving. In this case, the spectrum of the vortex contains an unstable mode with complex frequency which grows spontaneously; see, e.g., [6–12].

The possibility of stabilizing inherently unstable MQVs has been explored by using inhomogeneous trapping potentials to force the spatial distribution of superfluid matter [2] and by manipulating the superfluid via electromagnetic field fluctuations [13]. A third possibility is based on two-component condensates [14,15]. These systems can consist of different atoms [16], different isotopes of the same atom [17], or even different hyperfine states of the same isotope [18,19]. It has been suggested that in such systems [20–24] the overlapping second component can slow down or even prevent the decay of MQVs [5] of the first component. As we shall see, spatial separation is relevant to our problem. Two distinct modes of spatial separation exist [25,26]: Separation arising from the geometry of the trapping potentials, and separation resulting from the immiscibility of the two

*samuel_christian.patrick@kcl.ac.uk

†ansh.gupta@kcl.ac.uk

‡ruth.gregory@kcl.ac.uk

§carlo.barenghi@newcastle.ac.uk

components [27], a property characterized by the intercomponent interactions. Kuopanportti *et al.* [5] suggested how to stabilize MQVs in a tightly confined two-dimensional ^{87}Rb and ^{41}K mixture confined within a rotating harmonic trap. They successfully stabilized $\ell = 2$ MQVs with both attractive and repulsive intercomponent interactions by a clever distribution of the secondary component. In each case, the secondary component was distributed in such a way that the energetic favorability of MQV decay was not sufficient to overcome the intercomponent interactions: The MQVs were effectively “propped up” and could not decay. Unfortunately, the scope of this technique is limited by the tightness of the trapping potential: The vortex core was comparable in size to the size of the entire condensate.

In this work, we propose a method of stabilizing MQVs which exploits the spatial separation of mixtures with highly repulsive intercomponent interactions. We shall show that, by letting the second component concentrate inside the vortex core of the first component, the energetic advantage of vortex decay can be offset. To best facilitate stabilization of MQVs, it is paramount to choose a condensate mixture such that both components are self-repulsive and the intercomponent repulsion is large. A mixture of ^{87}Rb and ^{133}Cs atoms meets both requirements and is realizable in the laboratory [16]. Rather than a conventional harmonic trap, we consider the problem in a potential trap with a wide, flat bottom and steep walls, which allows for condensates that are homogeneous in the bulk [28,29]. The advantage of such large circular bucket potentials is that the vortex core profiles remain unchanged as they move about the condensate, unlike what happens in a tightly bound system, making our results independent of the trap’s details.

It has recently been argued that placing atoms of a second species inside the vortex core endows the vortex with a mass [30], such that the effective equations of motion for the vortex positions become second order in time derivatives (compared to the one-component case where they are only first order in time). This has been shown to have interesting consequences, such as radial oscillations of precessing vortices [31], reverse precession of a vortex in a harmonic trapping potential [32,33] and the recombination of nearby vortex pairs [34]. The latter is indicative of the stability of MQVs in two-component condensates. One of the principal aims of this work will be to elucidate the mechanism behind this enhanced stability. We go beyond the model presented in [31] by performing a full linear stability analysis that accounts for the dissipation of vortex energy into sound.

II. THE SYSTEM

A. Governing equations

The equations of motion of a trapped two-dimensional two-component condensate are

$$\begin{aligned} i\hbar\partial_t\Psi_1 &= [\hat{K}_1 + V(\mathbf{x}) + G_1|\Psi_1|^2 + G_{12}|\Psi_2|^2 - \tilde{\mu}_1]\Psi_1 \\ i\hbar\partial_t\Psi_2 &= [\hat{K}_2 + V(\mathbf{x}) + G_2|\Psi_2|^2 + G_{12}|\Psi_1|^2 - \tilde{\mu}_2]\Psi_2, \end{aligned} \quad (3)$$

where Ψ_j are the macroscopic wave functions for the components $j = 1, 2$, $\tilde{\mu}_j$ are the chemical potentials, $\hat{K}_j = -\frac{\hbar^2}{2M_j}\nabla^2$ are the kinetic energy operators, G_j are the two-dimensional

(2D) self-interaction parameters, and G_{12} is the 2D inter-species interaction parameter. The 2D trapping potential $V(\mathbf{x})$ [where $\mathbf{x} = (x, y)$] is taken to be a cylindrical box-trap of radius r_B and height V_0 . It is convenient to assume the circularly symmetric form

$$V(\mathbf{x}) = V(r) = \frac{V_0}{1 + (V_0 - 1)e^{a(r_B - r)}}, \quad (4)$$

where $r^2 = x^2 + y^2$. Assuming that V_0 is larger than both chemical potentials, the two species are essentially confined in the region $r < r_B$; within this region, $V(r)$ is negligible. The quantity a is a smoothing parameter. We assume the system is sufficiently low temperature that thermal noise and dissipation can be neglected. The assumption of an effectively two-dimensional system can be satisfied in practice by imposing a strong confinement of both components in the vertical direction, e.g., a harmonic potential with frequency $\omega_z \gg \tilde{\mu}_j/\hbar$, such that the dynamics in the extra dimension are frozen out (see Appendix A).

The system of equations (3) can be derived from the following action:

$$\mathcal{S} = \int dt d^2\mathbf{x} \left[\sum_j (i\hbar\Psi_j^*\dot{\Psi}_j - \mathcal{H}_j) - \mathcal{H}_I \right], \quad (5)$$

where the free-energy density for each component j and interspecies interaction energy density are defined, respectively, as

$$\begin{aligned} \mathcal{H}_j &= \Psi_j^*[\hat{K}_j + V(\mathbf{x}) - \tilde{\mu}_j]\Psi_j + \frac{G_j}{2}|\Psi_j|^4, \\ \mathcal{H}_I &= G_{12}|\Psi_1|^2|\Psi_2|^2. \end{aligned} \quad (6)$$

Since independent phase rotations of Ψ_1 and Ψ_2 are symmetries of \mathcal{S} , we obtain two conserved currents

$$\partial_t n_j + \nabla \cdot (n_j \mathbf{v}_j) = 0, \quad (7)$$

where $n_j = |\Psi_j|^2$ is the number density of component j , and $\mathbf{v}_j = \frac{\hbar}{M_j}\nabla \arg(\Psi_j)$ is its velocity. In a closed system, one can integrate over space to find that the number of atoms in each species, $N_j = \int n_j d^2\mathbf{x}$, is conserved by the evolution dictated by (3). Hereafter, we fix the number of atoms in the first component N_1 and treat $\eta = N_2/N_1$ as our variable.

An approximate expression for the ground-state solution of Eqs. (3) is provided by the Thomas-Fermi approximation: Neglecting the kinetic energy terms, within the trap [where $V(r) \simeq 0$] the steady-state solutions of (3) satisfy

$$G_1 n_1 + G_{12} n_2 - \tilde{\mu}_1 = 0, \quad G_2 n_2 + G_{12} n_1 - \tilde{\mu}_2 = 0. \quad (8)$$

Since the two components are immiscible for $G_{12} > \sqrt{G_1 G_2}$ [27], we can assume that component 2 is confined to the region $A_2 = \pi r_0^2$ and component 1 occupies the remaining space $A_1 = \pi(r_B^2 - r_0^2)$. We then have $n_1 = N_1/A_1$ and $n_2 = N_2/A_2$ so that the chemical potentials are approximately

$$\tilde{\mu}_1 = \frac{G_1 N_1}{A_1}, \quad \tilde{\mu}_2 = \frac{\eta G_2 N_1}{A_2}. \quad (9)$$

In this work, we consider systems with a vortex in Ψ_1 and no vortex in Ψ_2 . In the stationary state, solutions of (3) are of the

form

$$\Psi_1(r, \theta) = \sqrt{n_1(r)}e^{i\ell\theta}, \quad \Psi_2(r) = \sqrt{n_2(r)}, \quad (10)$$

where ℓ is the winding number of the vortex. The corresponding velocity field is $\mathbf{v}_1 = \frac{\hbar\ell}{M_1 r}\hat{\mathbf{e}}_\theta$, where $\hat{\mathbf{e}}_\theta$ is the unit vector in the azimuthal direction. For simplicity, we focus on the case $\ell = 2$; however, we expect our conclusions to extend to vortices of higher winding numbers. In particular, the stabilization mechanism we discuss in Sec. III B (which involves filling in the vortex core with a second component) will be qualitatively the same for different m and ℓ . The main difference will be that vortices with larger ℓ have a larger core region, hence we anticipate that more second components will be needed to stabilize the system in that case.

B. Dimensionless variables

In the rest of the paper, we express the governing equations (3) in dimensionless form using the following characteristic units of length, time, and density:

$$\xi_1 = \frac{\hbar}{\sqrt{\tilde{\mu}_{1,0}M_1}}, \quad \tau_1 = \frac{\hbar}{\tilde{\mu}_{1,0}}, \quad n_0 = \frac{\tilde{\mu}_{1,0}}{G_1}, \quad (11)$$

where $\tilde{\mu}_{1,0} = \tilde{\mu}_1(\eta = 0)$ is the chemical potential of species 1 in the vortex state when species 2 is absent. In other words, we perform the following rescalings:

$$\frac{r}{\xi_1} \rightarrow r, \quad \frac{t}{\tau_1} \rightarrow t, \quad \frac{V}{\tilde{\mu}_{1,0}} \rightarrow V, \quad \frac{\Psi_j}{n_0^{1/2}} \rightarrow \Psi_j, \quad (12)$$

so that (3) becomes

$$\begin{aligned} i\partial_t \Psi_1 &= \left[-\frac{1}{2}\nabla^2 + V(\mathbf{x}) + |\Psi_1|^2 + g_{12}|\Psi_2|^2 - \mu_1 \right] \Psi_1, \\ i\partial_t \Psi_2 &= \left[-\frac{1}{2m_2}\nabla^2 + V(\mathbf{x}) + g_2|\Psi_2|^2 + g_{12}|\Psi_1|^2 - \mu_2 \right] \Psi_2, \end{aligned} \quad (13)$$

where we have defined the new dimensionless parameters,

$$\mu_j = \frac{\tilde{\mu}_j}{\tilde{\mu}_{1,0}}, \quad g_2 = \frac{G_2}{G_1}, \quad g_{12} = \frac{G_{12}}{G_1}, \quad m_2 = \frac{M_2}{M_1}. \quad (14)$$

Note the true total number of atoms can be recovered from $N_j = \int d^3\mathbf{x}|\Psi_j|^2$ in these units by multiplying by a factor of $\hbar^2/M_1G_1 = d_1/\sqrt{8\pi}a_1$, where d_1 is the width of species 1 in the vertical direction, and a_1 is its scattering length (see Appendix A).

Since $\xi_1\ell$ (where ξ_1 is the healing length of the condensate 1 for $\eta = 0$) is the characteristic core size of an ℓ -vortex, in the new units the vortex core now has radius $\sim\ell$. Furthermore, since the density of condensate 1 approaches n_0 far from the vortex axis where $n_2 \rightarrow 0$, in the new units the bulk value of n_1 will approach μ_1 .

C. Parameters

In these units, the problem depends only on m_2 , g_2 , g_{12} , the parameters in the trapping potential, and the chemical potentials μ_j . The latter are related to the total number of atoms in the ground state (see the next section). The s -wave scattering lengths for the ^{87}Rb and ^{133}Cs mixture [35] are

$a_1 = 100a_0$, $a_2 = 280a_0$, and $a_{12} = 650a_0$ [26], where a_0 is the Bohr radius, and hereafter the subscripts 1 and 2 refer, respectively, to the ^{87}Rb and ^{133}Cs components. In Appendix A, we show that when both species are subject to the same strong vertical confinement, the dimensionless interaction parameters are $g_2 = 2.04$ and $g_{12} = 5.65$. The mass ratio is simply $m_2 = 133/87$. For the trapping potential, we fix $a = 5$ and $V_0 = 5$ so that there is essentially a hard wall located at $r = r_B$. For the trap radius, we pick $r_B = 40$ so that the trap is not too small to prohibit the instabilities under consideration but not so large that the problem becomes computationally impractical.

D. Stationary solutions

To solve for the stationary profiles $n_{1,2}$, we evolve (13) in imaginary time $\tau = it$. This amounts to making the replacement $i\partial_t \rightarrow -\partial_\tau$ in (3). Starting from a sensible initial condition, the population of the higher-energy modes will then decrease exponentially with increasing τ , leaving essentially only the ground state at late times. Since the anticipated densities are independent of the azimuthal coordinates, the speed of the computation is increased by working in polar coordinates. We therefore solve the following coupled set of equations,

$$\begin{aligned} \partial_\tau Y_1 &= \left(\frac{\nabla_r^2}{2} - \frac{\ell^2}{2r^2} - V(r) + \mu_1 - |Y_1|^2 - g_{12}|Y_2|^2 \right) Y_1, \\ \partial_\tau Y_2 &= \left(\frac{\nabla_r^2}{2m_2} - V(r) + \mu_2 - g_2|Y_2|^2 - g_{12}|Y_1|^2 \right) Y_2, \end{aligned} \quad (15)$$

where $\nabla_r^2 = \partial_r^2 + \frac{1}{r}\partial_r$ and $Y_j = |\Psi_j| = \sqrt{n_j}$. We work on a radial grid $r = [\Delta r, r_B + 5]$ with $\Delta r = 0.05625$ such that there are 800 radial points, and we use an imaginary time step $\Delta\tau = 4 \times 10^{-4}$. The evolution is performed using a fourth-order Runge-Kutta algorithm with the radial derivatives approximated using finite-difference stencils.

The first step is to fix a value for N_1 against which we can compare the effect of increasing η . This value is determined by solving (15) for $\eta = 0$, using the fact that $\mu_1(\eta = 0) = 1$, and integrating over the resulting profile to get $N_1 = \int d^2\mathbf{x}n_1(\eta = 0)$. For $r_B = 40$ and $\ell = 2$, we have $N_1 \simeq 4824$. Again, since this is the atom number in dimensionless variables, one must multiply by the dimensionless ratio $d_1/\sqrt{8\pi}a_1$ to find the true total number of atoms.

The second step is to choose an initial condition when the second component is added. We start by considering the case in which no vortex is present ($\ell = 0$) with component 2 localized in the center of the system and component 1 surrounding it. A subtlety of the problem is that if we want to keep $N_{1,2}$ fixed, the chemical potentials must vary to accommodate these constraints. *A priori*, we do not know the values of $\mu_{1,2}$ and must determine them during the imaginary-time evolution. We start by guessing their values using the Thomas-Fermi approximation (9), which in dimensionless units gives $\mu_1 = N_1/\pi(r_B^2 - r_0^2)$ and $\mu_2 = \eta g_2 N_1/\pi r_0^2$. Since we consider η to be very small, we take 1 as our initial guess for the value of μ_1 and invert the first relation to find the value of r_0 . The second relation provides a guess for μ_2 . The densities are then $n_1(r_0 < r < r_B) = \mu_1$ and $n_2(r > r_0) = \mu_2/g_2$. We

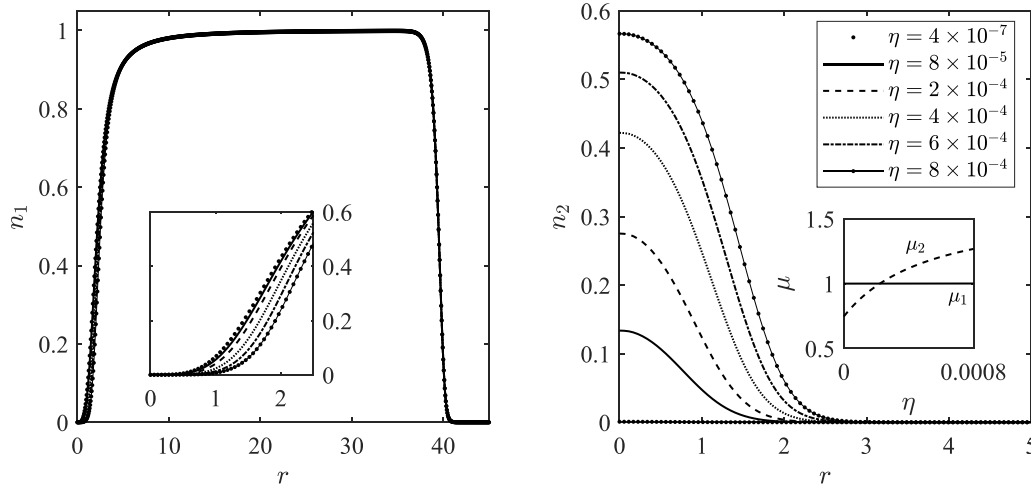


FIG. 1. Density profiles for species 1 (left) and species 2 (right) for various η values (indicated in the figure legend on the right). The vortex axis $r = 0$ is on the left and the trap's boundary is at $r = r_B = 40$. The other parameters are $\ell = 2$, and $N_1 \simeq 4824$ (the dimensionless number of atoms of species 1 when $\eta = 0$). The inset on the left panel shows a closeup of the vortex axis. Component 2 occupies the vortex core where the density of component 1 goes to zero. As the proportion of component 2 increases, the vortex core region widens. The inset on the right panel shows how the chemical potentials vary with η .

evolve these profiles forward in imaginary time, renormalizing $\Psi_{1,2}$ after each time step to keep the values of $N_{1,2}$ fixed. After a long time, the system will have relaxed to its lowest energy state; however, there will be residual time dependence due to the fact that the chemical potentials were chosen incorrectly. We can use this time dependence to infer the shift in μ_j using $Y_j(\tau + \Delta\tau) = e^{-\delta\mu_j\Delta\tau}Y_j(\tau)$, so that the true chemical potentials are $\mu_1 = 1 + \delta\mu_1$ and $\mu_2 = \eta g_2 N_1 / \pi r_0^2 + \delta\mu_2$, respectively. The evolution is terminated once the changes $\delta\mu_1$ and $\delta\mu_2$ over a time step are both less than 10^{-6} . This is suitably small given that $\mu_j \sim O(1)$ for both species, and it is computationally feasible when solving for a large range of η values.

In the third step, we imprint a vortex by setting $\ell \neq 0$ in (15), taking the ground states obtained from step 2 as the initial condition. We evolve again in imaginary time (using the same termination criterion) to find the stationary vortex solutions, and we update the chemical potentials accordingly.

In Fig. 1, we present the resulting density profiles $n_{1,2}$ as a function of r for a vortex with $\ell = 2$. We see that component 2 stays inside the core of the vortex in component 1, and its effect is to widen the core. It is remarkable that even the small values of η which we consider here have such a significant effect. This widening becomes more significant as η increases. We also display the variation of the chemical potentials with η in the inset of the right panel. μ_1 increases with η by a very small amount due to the repulsive effect of species 2 inside the vortex core. This forces more of the N_1 particles into the bulk of the condensate, increasing the mean value of the density in this region. μ_2 increases much more obviously with η since N_2 is increasing and therefore the density of species 2 must go up accordingly. Note, however, that μ_2 does not vanish as $\eta \rightarrow 0$. This is because there is a contribution of the curvature of n_2 to the chemical potential. Indeed, solving the equation in (15) for Y_2 in the limit $r \rightarrow 0$ gives the relation $\mu_2 = (g_2 n_2 - n_2'' / 2m_2 n_2)|_{r=0}$. This does not go to zero as $n_2 \rightarrow 0$ since the ratio n_2'' / n_2 stays finite in this limit.

III. LINEAR ANALYSIS

Having found the stationary vortex solutions to (13), we determine their stability by analyzing the normal modes of the system. It is well known that MQVs in one-component condensates spontaneously decay into clusters of SQVs and that this instability can be attributed to an unstable mode of the linearized equations of motion [8]. We now outline how this analysis can be extended to two-component condensates, and we demonstrate that, for sufficiently high values of η , this mode can be stabilized.

A. Bogoliubov method

Let $\delta\psi_j$ be small fluctuations about Ψ_j and write the following ansatz:

$$\begin{bmatrix} \delta\psi_1 \\ \delta\psi_2 \\ \delta\psi_1^* \\ \delta\psi_2^* \end{bmatrix} = \sum_{m=-\infty}^{\infty} e^{im\theta} \begin{bmatrix} u_1 e^{i\ell\theta} \\ u_2 \\ v_1 e^{-i\ell\theta} \\ v_2 \end{bmatrix}, \quad (16)$$

with u_j and v_j functions of r , t , and m , where m is the azimuthal wave number. When the equations of motion (13) are linearized, since neither $n_{1,2}$ nor $\mathbf{v}_{1,2}$ depends on θ , each m component evolves independently of the others. Due to the symmetries $u_j^*(m) = v_j(-m)$ and $v_j^*(m) = u_j(-m)$, we can restrict our attention to $m \geq 0$ modes without loss of generality. The fluctuations $|U\rangle = (u_1, u_2, v_1, v_2)^T$ obey the following coupled set of equations:

$$i\partial_t |U\rangle = \widehat{L} |U\rangle. \quad (17)$$

The operator \widehat{L} is

$$\widehat{L} = \begin{bmatrix} D_1^+ & \varepsilon & n_1 & \varepsilon \\ \varepsilon & D_2 & \varepsilon & g_2 n_2 \\ -n_1 & -\varepsilon & -D_1^- & -\varepsilon \\ -\varepsilon & -g_2 n_2 & -\varepsilon & -D_2 \end{bmatrix}, \quad (18)$$

where

$$D_1^\pm = -\frac{1}{2} \left[\nabla_r^2 - \frac{(\ell \pm m)^2}{r^2} \right] + V + 2n_1 + g_{12}n_2 - \mu_1,$$

$$D_2 = -\frac{1}{2M_2} \left[\nabla_r^2 - \frac{m^2}{r^2} \right] + V + 2g_2n_2 + g_{12}n_1 - \mu_2, \quad (19)$$

and the coupling between fluctuations of both species is determined by $\varepsilon = g_{12}\sqrt{n_1n_2}$. Note that for immiscible fluids, the region of overlap of the two components is small. ε will be small in this region and zero everywhere else. The fields u_j and v_j are related to the azimuthal Fourier components of the density field by

$$\delta n_{j,m} = \sqrt{n_j}(u_j + v_j), \quad (20)$$

such that when resumming over m , the complete density fluctuation is real-valued. The equations in (17) can be derived from the action $S_{\text{BdG}} = \int dt d^2\mathbf{x} \mathcal{L}_{\text{BdG}}$, where

$$\begin{aligned} \mathcal{L}_{\text{BdG}} &= iu_1^* \dot{u}_1 - iv_1^* \dot{v}_1 + iu_2^* \dot{u}_2 - iv_2^* \dot{v}_2 - \mathcal{H}_{\text{BdG}}, \\ \mathcal{H}_{\text{BdG}} &= \mathcal{H}_{\text{BdG},1} + \mathcal{H}_{\text{BdG},2} + \mathcal{H}_{\text{BdG,int}}, \\ \mathcal{H}_{\text{BdG},1} &= u_1^* D_1^+ u_1 + v_1^* D_1^- v_1 + n_1(u_1^* v_1 + u_1 v_1^*), \\ \mathcal{H}_{\text{BdG},2} &= u_2^* D_2 u_2 + v_2^* D_2 v_2 + g_2 n_2 (u_2^* v_2 + u_2 v_2^*), \\ \mathcal{H}_{\text{BdG,int}} &= \varepsilon [(u_1^* + v_1^*)(u_2 + v_2) + \text{c.c.}]. \end{aligned} \quad (21)$$

S_{BdG} is invariant when each of the fields u_j and v_j simultaneously undergoes the same phase rotation. The corresponding conserved quantity is the Bogoliubov norm,

$$\mathcal{N}_{\text{BdG}} = \langle U | \gamma^0 | U \rangle \equiv \sum_j \int d^2\mathbf{x} (|u_j|^2 - |v_j|^2), \quad (22)$$

where $\gamma^0 = \text{diag}(1, 1, -1, -1)$ is the zeroth gamma matrix. Notice that due to the presence of the cross-terms with coefficient ε in (21), excitations of species 1 can be converted into excitations of species 2 and vice versa. However, the total number of excitations, as measured by \mathcal{N}_{BdG} , is conserved.

Since the background is stationary, we can further decompose the fluctuations into the separate frequency components,

$$|U(r, t)\rangle = \int_{-\infty}^{\infty} \frac{d\omega}{2\pi} a_\omega(t) |\tilde{U}(r; \omega)\rangle, \quad (23)$$

where a_ω and $|\tilde{U}\rangle$, respectively, satisfy

$$i\partial_t a_\omega = \omega a_\omega, \quad \omega |\tilde{U}\rangle = \hat{L} |\tilde{U}\rangle. \quad (24)$$

The first equation is solved by $a_\omega \propto e^{-i\omega t}$ up to an arbitrary constant, while the second must be solved numerically. The Hamiltonian for stationary modes is related to the Bogoliubov norm via $H_{\text{BdG}} = \int d^2\mathbf{x} \mathcal{H}_{\text{BdG}} = \omega \mathcal{N}_{\text{BdG}}$. Therefore, a positive frequency mode with negative norm (or a negative frequency mode with positive norm) has negative energy. The sign of the energy plays an important role in the discussion of the instability.

To solve the second equation in (24) computationally, we write the radial derivative terms using finite-difference stencils on a discrete r -grid, and then find the eigenvalues and eigenfunctions of the resulting matrix \hat{L} . The eigenfunctions are normalized so that $|\text{Re}[\mathcal{N}_{\text{BdG}}]| = 1$, which gives an unambiguous normalization condition for all solutions obtained.

We place a Dirichlet boundary condition at large r , although this does not play a significant role as it is applied in a region where $V(r)$ is large, hence modes with energy lower than the barrier height quickly decay to zero inside this region. A discussion of the boundary conditions at $r = 0$ can be found in Appendix B.

In Fig. 2, we present the eigenvalues ω as a function of η for $\ell = 2$ and $r_B = 40$. There are two distinct types of excitation. Bulk excitations (shown in black) predominantly occupy the region outside of the vortex core and are associated with collective excitations of the condensate or phonons at low wave numbers. Indeed, in panel (c), it can be seen that these modes have a large oscillatory component in the large- r region. They have positive energy ($H_{\text{BdG}} > 0$) and are largely unaffected by increasing η , which influences only the vortex core. There is a second class of excitation, which we refer to as vortex modes. These have negative energy ($H_{\text{BdG}} < 0$) at low η and are mainly localized around the vortex axis, as illustrated in panel (c). In panel (a), we see that there is only one such mode for the $\ell = 2$ vortex represented by the red line. Since this mode occupies the same region as component 2, it is strongly affected when η is increased. Indeed, the frequency of the vortex mode in panel (a) can be seen to decrease rapidly even for relatively small amounts of component 2. In the presence of a dissipation mechanism, these modes will be excited since they lower the total energy of the system, i.e., they are an energetic instability.

When $\text{Re}[\omega]$ of the vortex mode crosses that of a bulk excitation, the two couple to produce a complex-conjugate pair of modes with vanishing Bogoliubov norm. This leads to the appearance of isolated bubbles in $\text{Im}[\omega]$ in panel (b). The mode with $\text{Im}[\omega] > 0$ represents a dynamical instability, that is, the central vortex spontaneously sheds its energy into a sound wave in the bulk even without a dissipation mechanism. This does not violate energy conservation since the total energy of the mode encoding this behavior is zero ($H_{\text{BdG}} = 0$). The complex-conjugate mode describes the time-reversed process, i.e., absorption of a sound wave by the central vortex. In panel (d), we show how the waveforms of the two modes in panel (c) combine to produce the real and imaginary parts of the instability.

Note that for large enough r_B (larger than considered here), i.e., in the limit in which finite-size effects become negligible, the bubbles in $\text{Im}[\omega]$ eventually merge into a continuum [10]. In that case, there is a dynamical instability at $\eta = 0$ for all larger trap sizes and, in particular, in the infinite system limit.

We also show in Fig. 3 the effect of increasing η on the waveform of the vortex mode around the vortex axis. The main feature is that the amplitude of the mode at $r = 0$ is suppressed as the number of atoms in species 2 is increased. This will be addressed in the next section.

For large η , the vortex mode has a frequency lower than all positive frequency bulk excitations. At a critical η value, which we call η_c [the black dot in Fig. 2(a)], the frequency of the vortex mode changes sign. Since the Bogoliubov norm of this mode is negative, the energy of the vortex mode is positive for $\eta > \eta_c$ and it will no longer get excited when a dissipation mechanism is included. Furthermore, since the negative frequency bulk excitations have negative norm, they have positive energy and the vortex mode cannot mix with

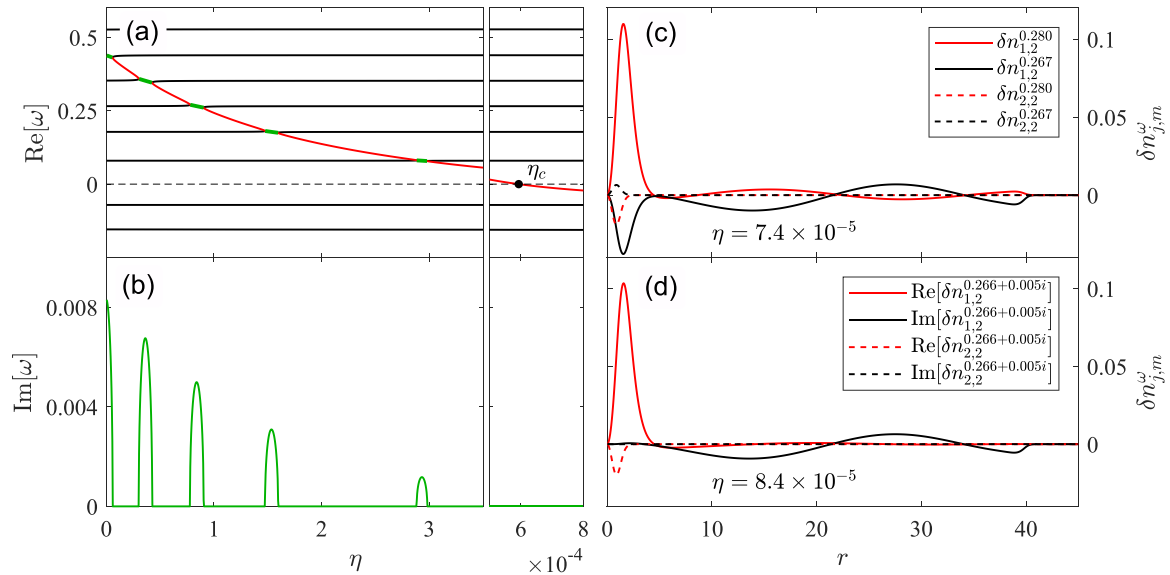


FIG. 2. On the left, we display the eigenvalues ω of (17) as a function of η for $m = \ell = 2$ and $r_B = 40$, with the real part in panel (a) and the imaginary part in panel (b). For clarity, both panels (a) and (b) are split into two regions for small and large values of η . The modes whose frequency is approximately independent of η (solid black horizontal lines) are bulk excitations (phonons) which are not affected by component 2 in the vortex core. The mode whose frequency decreases with η (solid red) is an excitation of the vortex core and has negative norm for all frequencies. When the vortex mode crosses a bulk excitation mode, the two modes couple with each other to produce a pair of complex conjugate modes (solid green) with zero norm and complex frequency ω . At a critical value η_c (marked as a solid black dot), the frequency of the vortex mode (red line) changes sign. On the right, we display some example mode functions for the vortex mode. In panel (c), we pick an η value slightly to the left of the third instability bubble in panel (b). The solid black (red) curve corresponds to the bulk (vortex) excitations of component 1 with the frequency indicated. The dashed curves of the same color correspond to component 2. In panel (d), we pick the η value at the peak of the third instability bubble and display the real and imaginary parts of the growing mode. Comparing panels (c) and (d), we see that the vortex mode enters mainly the real part of the unstable eigenmode while the bulk excitation is captured by the imaginary part. Time evolution then causes these waveforms to rotate into each other via the factor $e^{-i\omega t}$ multiplying them, which is a manifestation of the coupling between vortex mode and bulk excitation.

these modes to produce a dynamical instability with zero energy. Above η_c , the system is stabilized by the presence of the second component. This stabilization will also occur in an infinite system. Although the phonon spectrum is continuous in that case, what is relevant is that when the system crosses η_c , the vortex mode energy is not the correct sign to produce an eigenmode with complex frequency. In that case, we expect there to be a series of avoided crossings with the $\omega < 0$ phonons, although an explicit demonstration is beyond the computational grid sizes probed in this work. The next section will explore the mechanism underpinning this stabilization, while Sec. IV will demonstrate stability via a full numerical simulation of (13).

From Fig. 2(a), we find the value $\eta_c = 5.933 \times 10^{-4}$. Since the value obtained will depend in general on the resolution used in the numerics, we estimate that the infinite resolution limit would yield the value $\eta_c = 5.936 \times 10^{-4}$ (details are in Appendix C). Note that this value is also specific to an $\ell = 2$ vortex in a trap of a radius $r_B = 40$ and will in general depend on both these parameters. Due to computational cost, we do not study this dependence here.

A computation of the mode energy in (21) gives insight into the behavior around η_c . In Fig. 4, we integrate the (vortex mode) energy density components in (21) over space and plot as a function of η . The total energy H_{BdG} is negative at low η except inside finite windows where it is vanishing due to the dynamical instability. At the edge of these windows, the

amplitudes of the normalized mode diverge, as reflected in the components of H_{BdG} , but they do so in a way that keeps the total energy finite. The energy of species 2 fluctuations $H_{\text{BdG},2}$ is always positive while the interaction energy $H_{\text{BdG,int}}$ between fluctuations of each species is always negative. The energy of species 1 fluctuations $H_{\text{BdG},1}$ is initially negative but becomes positive around $\eta = 2.33 \times 10^{-4}$. Correspondingly, the maximum amplitude of the vortex mode waveform shifts outwards into a region where it has positive energy density (see Fig. 3). Since $H_{\text{BdG,int}}$ is close to the value of $-2H_{\text{BdG},2}$, the total mode energy is still negative even when $H_{\text{BdG},1} = 0$. Interestingly, in this regime, the energetic instability of the vortex mode is a result of the interaction between fluctuations of the two species, rather than being an inherent property of the vortex in species 1 alone. Increasing η further, the total energy changes sign at η_c . This coincides with $H_{\text{BdG},1}$ exceeding the value of $H_{\text{BdG},2}$.

B. WKB method

To interpret why the vortex mode is shifted to lower frequency with increasing η , we apply a WKB method. This method has been demonstrated to give insight into the physical origin of vortex instabilities [11] as well as providing reasonable estimates of the unstable mode frequencies [12]. Following the procedure outlined in [12], we first write a

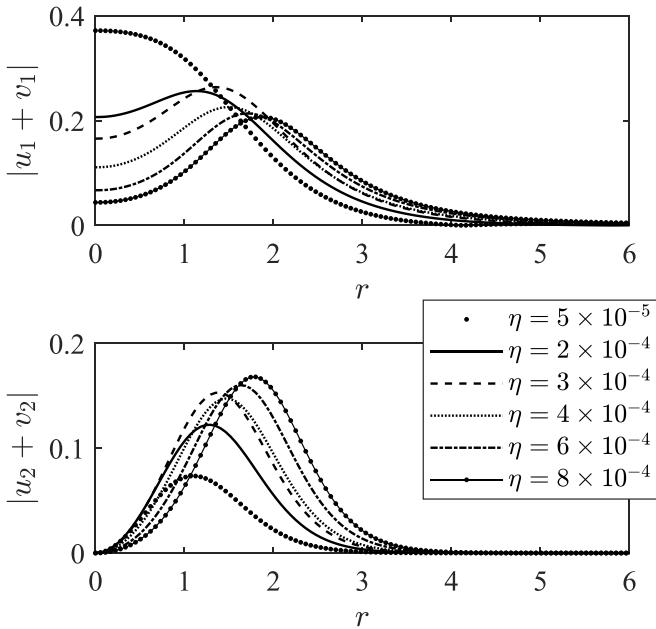


FIG. 3. Variation of the vortex mode waveform with η . In particular, we display the modulus of $u_j + v_j$, which is the combination appearing in formula (20) for density fluctuations. The main effect of the second component is to reduce the amplitude of excitations of species 1 on the vortex axis. The shift in the maximum of $|u_1 + v_1|$ between $\eta = 2 \times 10^{-4}$ and 3×10^{-4} is responsible for $\mathcal{H}_{\text{BdG},1}$ becoming positive in Fig. 4, since the waveform moves into a region of positive energy density.

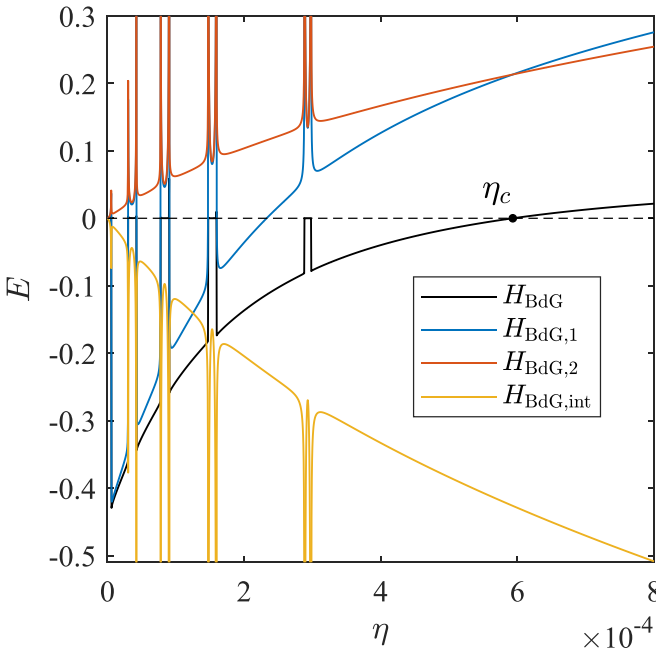


FIG. 4. Vortex mode energy densities in (21) integrated over space. The total energy smoothly increases from negative to positive, except in finite windows where it vanishes due to the dynamical instability. The change in sign of the total energy is associated with the energy of fluctuations in species 1 exceeding that of species 2.

WKB ansatz,

$$\begin{bmatrix} u_j \\ v_j \end{bmatrix} = \begin{bmatrix} \mathcal{A}_j(r) \\ \mathcal{B}_j(r) \end{bmatrix} e^{i \int p(r) dr}, \quad (25)$$

where p is the local component of the wave vector in the radial direction, and we assume $|p^2| \gg |\partial_r p|$, $|p \mathcal{A}_j| \gg |\partial_r \mathcal{A}_j|$, and similarly for \mathcal{B}_j . Taking only the leading-order contributions and eliminating the four amplitudes, Eq. (24) becomes

$$\mathcal{D}_1(k_1) \mathcal{D}_2(k_2) = \varepsilon^2 k_1^2 k_2^2, \quad (26)$$

where

$$\begin{aligned} \mathcal{D}_1(k_1) &= \Omega^2 - n_1 k_1^2 - k_1^4/4, \\ \mathcal{D}_2(k_2) &= \omega^2 - g_2 n_2 k_2^2 - k_2^4/4, \end{aligned} \quad (27)$$

and $\Omega = \omega - m\ell/r^2$ is the frequency in the frame rotating with the vortex. We have also defined a pair of effective wave vectors by

$$k_1^2 = p^2 + \frac{\tilde{m}_1^2}{r^2}, \quad M_2 k_2^2 = p^2 + \frac{\tilde{m}_2^2}{r^2}, \quad (28)$$

where the effective azimuthal numbers are

$$\begin{aligned} \tilde{m}_1^2 &= m^2 + \ell^2 + 2r^2(n_1 + g_{12}n_2 - \mu_1), \\ \tilde{m}_2^2 &= m^2 + 2M_2 r^2(g_2 n_2 + g_{12} n_1 - \mu_2). \end{aligned} \quad (29)$$

Hence, we can identify the condition in (26) as two coupled dispersion relations describing excitations of components 1 and 2, respectively, interacting through a small overlap region where ε is nonzero. As a first approximation, we study the noninteracting case with $\varepsilon \rightarrow 0$. We are particularly interested in the fluctuations of component 1 (since this is where the instability arises) which approximately satisfy $\mathcal{D}_1(k_1) \simeq 0$. This condition has two sets of solutions for p that are decoupled from each other. The first type are evanescent over the whole system, whereas the second can propagate. We are only interested in the second type. These are determined by

$$p^2 + W_+ = 0, \quad W_+ = -2\sqrt{n_1^2 + \Omega^2} + 2n_1 + \frac{\tilde{m}_1^2}{r^2}. \quad (30)$$

Points where $p = 0$ correspond to turning points, i.e., radial locations where an incoming wave instantaneously comes to rest before reversing its direction and propagating back out [12]. We can therefore view W_+ as an effective potential; when $W_+ < 0$ these waves are propagating, while for $W_+ > 0$ they are evanescent.

To see the effect of adding a second component, one can expand the \tilde{m}_1^2 term in W_+ :

$$W_+ = -2\sqrt{n_1^2 + \Omega^2} + 4n_1 - 2\mu_1 + \frac{m^2 + \ell^2}{r^2} + 2g_{12}n_2. \quad (31)$$

In the absence of the second component, this potential has a cavity located about $r = 0$ where waves with correct frequency can become trapped as bound states. These states approximately satisfy $\cos I \simeq 0$ [12], where $I = \int_{\text{cav}} p dr$ is the phase integral inside the cavity in the vortex core (see Appendix D for a further discussion). When a second species is present inside the vortex core, the final term in (31) creates a bulge in the potential around $r = 0$ (as shown in Fig. 5),

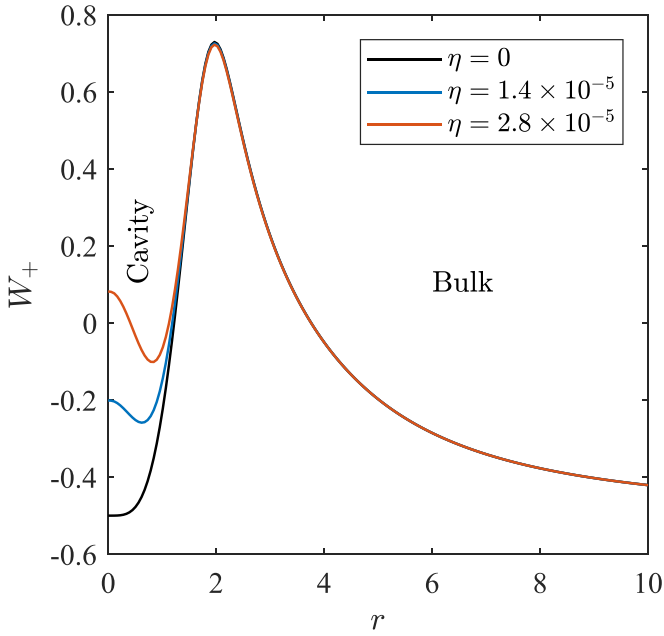


FIG. 5. The potential W_+ from (31) with $m = \ell = 2$ for an example frequency $\omega = 0.75$. In the WKB approximation, excitations of component 1 propagate when $W_+ < 0$. Excitations of the vortex are bound states inside the cavity centered on the axis, and they correspond to the central vortex splitting into a cluster. A second component in the vortex core induces a bulge in the cavity, decreasing the amount of space for vortex excitations. As the bulge grows in size, the vortex excitation decreases its frequency until, for large enough η , there are no positive frequency modes that fit inside the cavity.

thereby decreasing the amount of space the mode has to fit in the cavity. This bulge inhibits wave propagation in the immediate vicinity of the vortex axis, explaining the feature of Fig. 3 where the amplitude of the waveform drops on the vortex axis with increasing η . Conventional wisdom gained from the 1D Schrödinger equation in quantum mechanics would dictate that this should raise the frequency of the bound state, but this is not the case here, as we now illustrate.

To solve the resonance condition in the cavity, one should compute $I(\omega)$ for all frequencies that probe the cavity before finding the one that solves $\cos I = 0$. For small η , we show in Appendix D that the integral near the bottom of the cavity (for $m = \ell = 2$) can be expanded as

$$I(\omega) = \frac{\pi(\omega_0 - \omega)}{|2g_{12}n''_{2,0}|^{1/2}} + O[(\omega_0 - \omega)^2], \quad (32)$$

where ω_0 is the maximum frequency that probes the cavity, and $n''_{2,0}$ is the curvature of the density of component 2 on the axis. This expression demonstrates that I decreases as ω increases, i.e., $\partial_\omega I < 0$. More generally, the reason for this difference with the standard Schrödinger picture (in which $\partial_\omega I > 0$) is that the vortex mode in the WKB picture is on the lower branch of the dispersion relation where $\Omega < 0$ (which is related to the negative norm of the mode). On this branch, the root with $p > 0$ has negative group velocity $\partial_p \omega < 0$, i.e., decreasing ω increases the value of p . Therefore, since increasing η will decrease p through the final term in (31), the

frequency of the bound state decreases to keep I fixed at the value satisfying the resonance condition.

Although the WKB method correctly predicts the decrease of the vortex mode frequency with increasing ω , it fails at providing the quantitative value. This is to be expected since the approximation works best for high frequencies in regions where the background functions change gradually. Indeed, in [12], the WKB estimates are practically indistinguishable from numerical calculations for bulk excitations, while for the vortex mode (which occupies a region where the background density quickly changes) the WKB estimate differs notably from the numerics. When $\eta \neq 0$, the frequency is lower than the $\eta = 0$ case and the bulge in W_+ makes background variations more significant. Both of these features decrease the quantitative power of the WKB approximation.

IV. NUMERICS

Having gained an understanding of the instability mechanism from the linear theory, we now perform a series of fully nonlinear simulations of (13). The first goal will be to demonstrate explicitly the stabilization mechanism, showing that for high η values the $\ell = 2$ vortex fails to split. We then move on to discuss a by-product of the stabilization mechanism: The counter-rotating orbital motion of a pair of corotating vortices.

A. One component

We first evolve (3) for $\eta = 0$, i.e., when the second species is absent. For our spatial grid, we take $x \in [-(r_B + 5), r_B + 5]$ and similarly for y with $N = 512$ spatial points. We take $\Delta t = 5 \times 10^{-3}$ and evolve using a split-step Fourier method for 2×10^5 steps in time, saving every 200th frame. For the initial condition, we seed the stationary vortex profile for $\ell = 2$ and $r_B = 40$ with the unstable mode of amplitude $|a_\omega(t = 0)| = 10^{-3}$. We note that the corresponding resolution in the radial direction is 256 points, which differs from the value of 800 used in Sec. IID. The reduced resolution slightly shifts the location of the instability bubbles in Fig. 2. Hence, for consistency, we repeat the procedure in Secs. IID and IIIA for $\Delta \tau = 5 \times 10^{-3}$ and 256 radial grid points when producing the initial condition, since we want to precisely seed the mode that is unstable in our nonlinear simulations. A comparison of the normal mode spectra at different resolutions can be found in Appendix C.

The results are shown in Fig. 6. Panels (a)–(c) show the density at early, intermediate, and late times, with constant density contour superimposed in red/white, and panels (d)–(f) show the phase at the same times. In panels (a) and (d) the vortex is close to its stationary profile, while in panels (b) and (e) a deformation of the central vortex can be seen. In panels (c) and (f) the central vortex has split into two $\ell = 1$ vortices. The density contours indicate that this splitting is accompanied by the production of a bulk excitation, namely a sound wave with $m = 2$. At sufficiently late times, the vortices move back into the center due to finite system effects studied in [11]. Since our focus is on the splitting mechanism, we do not discuss this behavior further here. In the presence of dissipation, the initial splitting described here continues and the vortices separate widely, as we show in Sec. IVD.

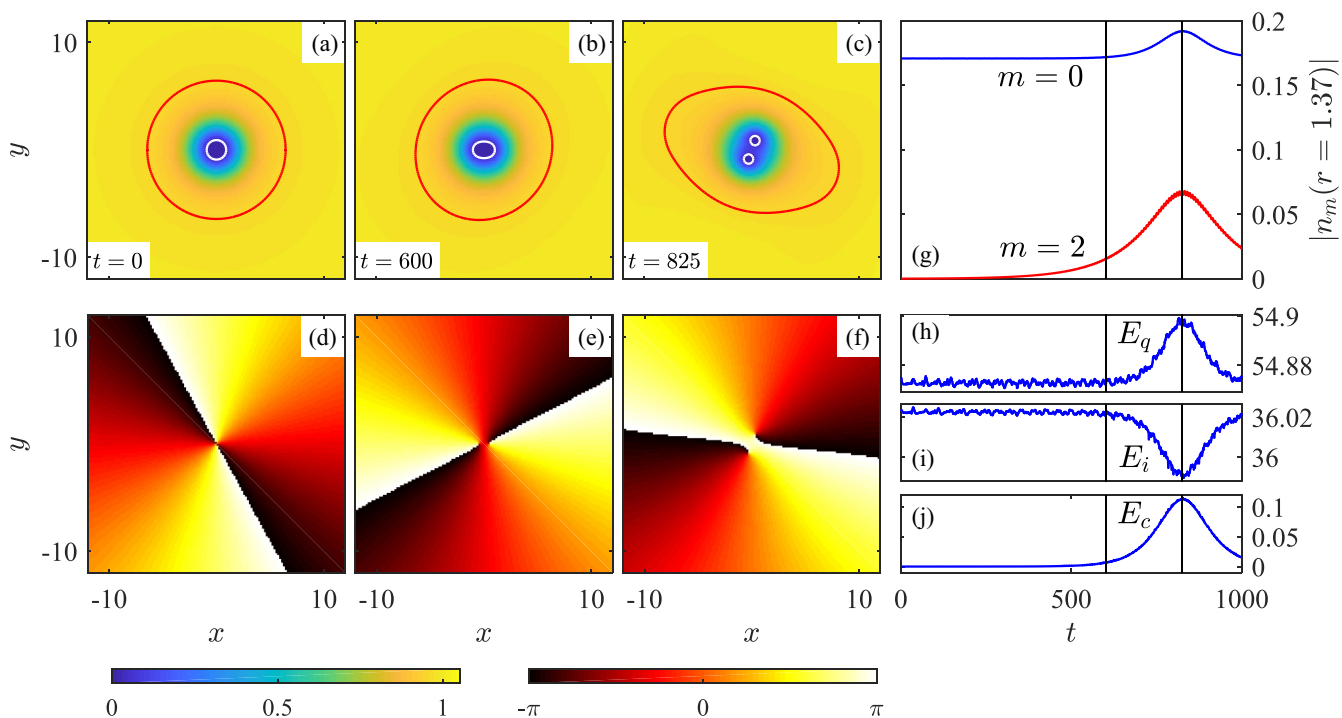


FIG. 6. Splitting of a vortex with $\ell = 2$ when $\eta = 0$. The density is displayed in panels (a)–(c) at three different times. The constant density contours are set at 0.95 (red outer contour) and 0.05 (white inner contours). These help indicate the vortex splitting and the production of an $m = 2$ sound wave in the bulk of the condensate. Panels (d)–(f) indicate the phase at the same times. In panel (g), we show the variation of the modulus of the $m = 0$ and 2 Fourier components of the density with time. The $m = 2$ mode grows exponentially before saturating and decaying due to finite-size effects [11]. The vertical black lines indicate the times $t = 600, 825$. We display various components of the energy in panels (h)–(j), showing that the vortex splitting is associated with a decrease (increase) in incompressible (compressible/quantum) energy.

In panel (g), we perform a Fourier decomposition of the density $n = (2\pi)^{-1} \int d\theta e^{im\theta} n_m$ [36] and display modulus of the Fourier components $m = 0, 2$ at the location $r = 1.37$. This location corresponds to the peak of the radial waveform $n_{m=2}(r)$. At first, the $m = 2$ mode grows exponentially in line with the prediction of Fig. 2. Around $t = 800$, the $m = 2$ mode reaches a maximum amplitude and starts to decay as the vortices move back into the center. Near the maximum amplitude of $n_{m=2}$, we also observe the nonlinear effect of the unstable mode on the $m = 0$ component. This is simply the backreaction of the growing mode onto the background density profile, which can be physically understood as the condensate filling in the center as the vortices move apart.

The instability is associated with a decrease of incompressible (vortex) energy and an increase in compressible (sound wave) energy. The energy of the system can be decomposed as

$$E = E_{\text{kin}} + E_q + E_{\text{pot}} + E_{\text{int}}, \quad E_a = \int d^2\mathbf{x} \mathcal{E}_a, \quad (33)$$

$$\mathcal{E}_{\text{kin}} = \frac{1}{2} n |\nabla \Phi|^2, \quad \mathcal{E}_q = \frac{1}{2} |\nabla \sqrt{n}|^2,$$

where the kinetic energy E_{kin} is associated with a nonvanishing velocity field and the quantum energy E_q results from density variations. $\mathcal{E}_{\text{pot}} = Vn$ and $\mathcal{E}_{\text{int}} = n^2/2$ are the usual potential and interaction energy densities, respectively. The kinetic energy can be further split into compressible and incompressible parts by defining $\mathbf{u} = \sqrt{n} \nabla \Phi$ and writing $\mathbf{u} = \mathbf{u}_c + \mathbf{u}_i$, where the incompressible part obeys $\nabla \cdot \mathbf{u}_i = 0$.

Operationally, the compressible part can be found by performing a Fourier transform \mathcal{F} , projecting \mathbf{u} onto the wave vector \mathbf{k} , and computing the inverse Fourier transform \mathcal{F}^{-1} . That is, $\mathbf{u}_c = \mathcal{F}^{-1}[\mathbf{k}(\mathbf{k} \cdot \mathcal{F}\mathbf{u})/|\mathbf{k}|^2]$ and $\mathbf{u}_i = \mathbf{u} - \mathbf{u}_c$. Since \mathbf{u}_c and \mathbf{u}_i have zero overlap, the kinetic energy can be written $E_{\text{kin}} = E_c + E_i$, with $E_c = \int d^2\mathbf{x} \mathcal{E}_c$ and similarly for E_i . We display E_q , E_i , and E_c in panels (h), (i), and (j), respectively. The incompressible energy decreases as the vortices move apart (into a lower-energy configuration) and the compressible and quantum energies increase in response. The two vertical black lines in the rightmost panels correspond to the times in panels (b) and (c), respectively.

B. Two components

To assess the effect of adding a small amount of component 2 inside the vortex core of component 1, we repeat the simulation of the last section for various values of η . In particular, we start from the stationary profiles for condensates 1 and 2 and perturb the system by inserting the unstable mode with an amplitude 10^{-3} . The values of η chosen correspond to the peaks of $\text{Im}[\omega]$ in the stability windows at the chosen resolution.

In Fig. 7, we display the densities of species 1 and species 2 for four values of η at the same times depicted as the $\eta = 0$ case in Fig. 1. As η increases, we clearly see that the vortices have separated less at a given instant of time when compared with the single-component system, thereby demonstrating the stabilizing effect of the second species.

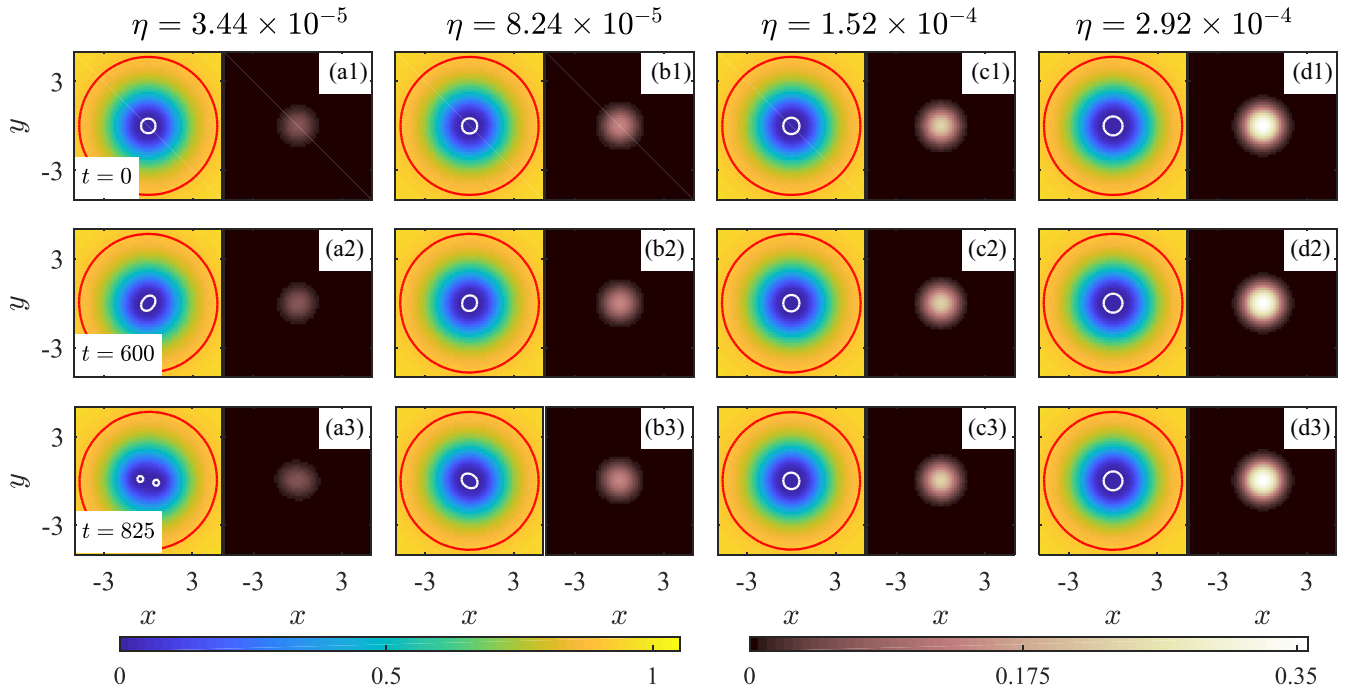


FIG. 7. The densities $n_{1,2} = |\Psi_{1,2}|^2$ for various η at the same times shown in Fig. 1. In each panel, the density of component 1 is shown on the left (corresponding color bar, bottom left) and component 2 on the right (bottom right). The constant density contours for component 1 are set at 0.9 (red outer contour) and 0.005 (white inner contours) and help indicate the vortex splitting. As η is increased, the central vortex in component 1 is less deformed at a given time, while the density of component 2 increases, becoming more and more visible on the color scale.

Since the minute separation becomes less and less transparent from the density plots with increasing η , we show in Fig. 8 the growth of the $m = 2$ mode in the vortex core. Here, we clearly

see that both the oscillation frequency and the growth rate decrease with increasing η . The values of $\text{Re}[\omega]$ and $\text{Im}[\omega]$ correspond to those predicted by the linear analysis in Fig. 2 (see Appendix C for an explicit comparison).

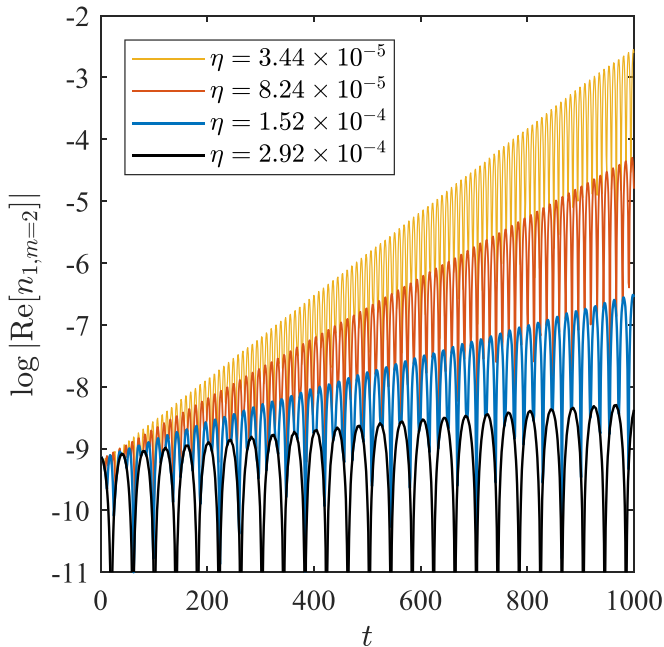


FIG. 8. Growth of the $m = 2$ unstable mode for various η values. For each η , we look at the time dependence of the mode at the spatial location where $n_{1,m=2}$ has maximum amplitude (which is around $r \sim 1.6$ – 1.9). As η increases, the oscillation frequency and growth rate decrease in accordance with the linear prediction of Fig. 2.

C. Orbit reversal

In general, the unstable mode in the spectrum of the MQV is associated with its splitting into a cluster of SQVs, whose distribution is determined by the m -fold symmetry of the unstable mode. In single-component systems, the cluster rotates in the direction of the net winding of the system, since each vortex essentially moves under the collective influence of all the others. The story is not so simple when a second component is added. The orbital frequency of the resulting cluster is given by $\text{Re}[\omega]/m$, with $\text{Re}[\omega]$ the oscillation frequency of the unstable mode. Hence, the frequency inversion for $\eta > \eta_c$ seen in Fig. 2 is associated with the reversal of the cluster's orbital motion. We demonstrate this now with a numerical simulation.

We choose a series of η values where the vortex is dynamically stable. Note here that dynamical stability below η_c results from finite-size effects for certain ranges of r_B , while above η_c it persists for all trap sizes, as shown by Fig. 2. Using the same resolution as the previous section, we now seed the stationary vortex profile with the vortex mode of amplitude $|a_\omega(t=0)| = 2$. Due to the large amplitude, in all cases we observe a sudden burst of sound from the central vortex as the system relaxes through nonlinear interactions. After this initial burst, we observe a stably orbiting vortex pair in the center of the trap surrounded by small noise. In Fig. 9, we display snapshots of the density profiles of the two species at

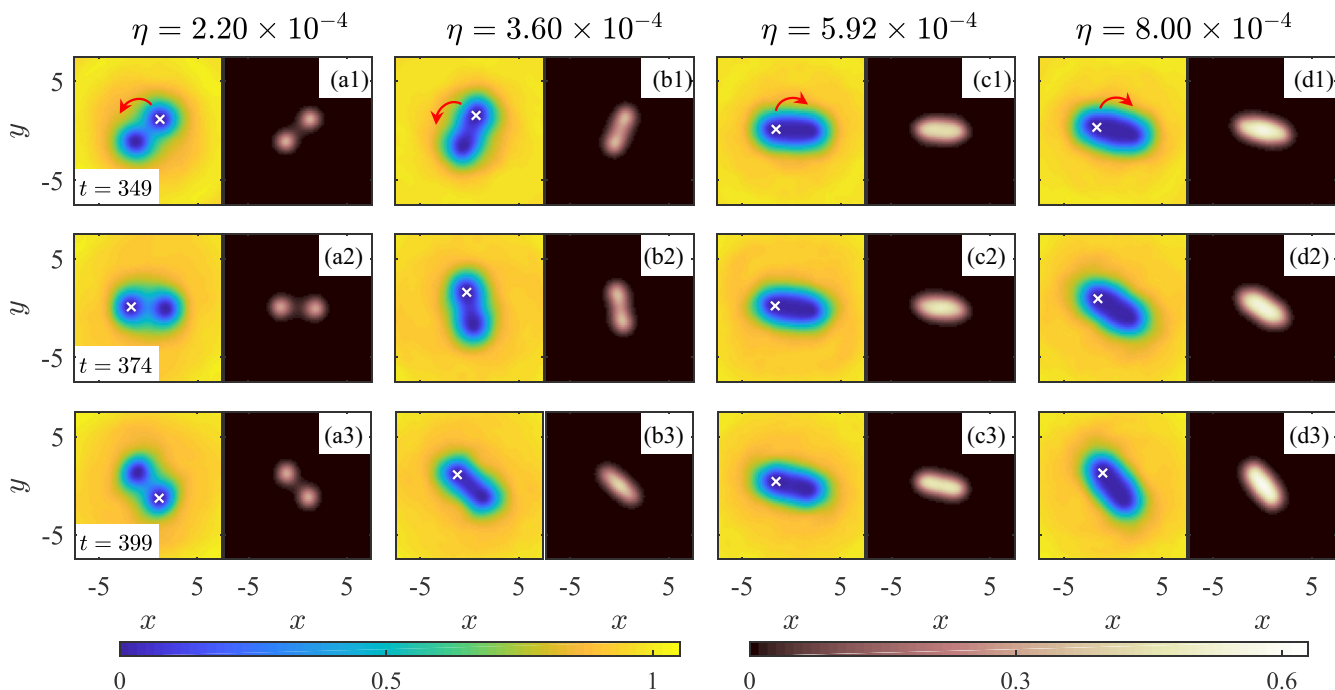


FIG. 9. Vortex pair motion for various η values at three different times. In each of the four columns, the left plot depicts $|\Psi_1|^2$ (color bar bottom left) and the right plot $|\Psi_2|^2$ (color bar bottom right). Each row corresponds to the time indicated on the left. The direction of the vortices is indicated with a red arrow, and one of the vortices is marked with a white cross to help illustrate the motion. In panels (a1)–(a3) the pair complete less than half a full orbit in the counterclockwise sense between each snapshot. In panels (b1)–(b3) the motion is also counterclockwise with lower orbital frequency. In panels (c1)–(c3) the motion is clockwise with low orbital frequency, and in panels (d1)–(d3) the motion is clockwise and slightly faster. The change in direction of the orbit is associated with a low-density region between the vortex pair in component 1 and a high-density region in the same area in component 2.

three different times. The red arrows indicate the direction of the orbital motion. For the two leftmost columns, the orbital motion is counterclockwise, corresponding to $\text{Re}[\omega] > 0$ for the vortex mode below η_c . The atoms of species 2 are shared between the two $\ell = 1$ vortices in the pair and track their motion. Conversely, the orbital motion is clockwise on the two rightmost columns, corresponding to $\text{Re}[\omega] < 0$ above η_c .

For large η we find that a region of depleted density in component 1 persists between the two separated vortices and is occupied by component 2. We interpret this as the result of the waveforms in Fig. 3. For $\eta = 0$, the maximum value of the waveform on the vortex axis nonlinearly excites the $m = 0$ mode as the vortices separate, causing atoms to fill in the space between them. For large η , the waveform decreases approaching $r = 0$, suppressing the nonlinear excitation of $m = 0$ in that region. Physically, the presence of component 2 on the vortex axis prevents excitations in component 1 propagating there, which means there is nothing to increase the value of the density of component 1 at $r = 0$ as the vortices separate.

D. Dissipation

In the presence of a dissipation mechanism, an MQV in a one-component condensate will still decay even if the vortex mode does not couple to any bulk excitations. The reason is that the vortex mode has negative energy, hence its excitation lowers the total energy of the system, as required by the dissipation. The same is not necessarily true in a two-component

system, as we now show, since the vortex mode has a positive energy above η_c .

In Fig. 10, we present results of three simulations performed with damping. The initial conditions in panels (a), (b), and (c) are, respectively, the final frames of the simulations shown in Figs. 7(a), 9(a), and 9(d), corresponding to the same η values indicated at the top of the figures. These correspond, respectively, to the lowest fraction of η simulated, which are unstable [panel (a)] and stable [panel (b)] when $\gamma_1 = 0$, and the largest η value simulated above η_c [panel (c)]. As η is small, damping applied to atoms of the second species will quickly reduce N_2 to zero. Hence, we only apply damping to the first component. This is achieved by replacing $i\partial_t$ by $(i - \gamma_1)\partial_t$ in (13), taking the value $\gamma_1 = 5 \times 10^{-2}$.

In Figs. 10(a1)–10(a3), the initial condition is a dynamically unstable vortex mode with low amplitude. In the three snapshots, we observe the central MQV splitting into a pair of SQVs rotating counterclockwise with equal amounts of second component in the two cores. During the splitting, the second species remains confined to the vortex cores, rather than being dispersed across the system.

In panels (b1)–(b3), the initial condition is two nearby SQVs surrounded by noise. The noise is quickly damped out and the vortices spiral out in the counterclockwise sense with decreasing orbital frequency. In this regime, the vortices orbit in accordance with the regular point-vortex dynamics [1], which dictates that the orbital frequency is approximately $\Omega = 2/s^2$, where s is the separation between vortices, with the atoms of species 2 playing a negligible role in the dynamics.

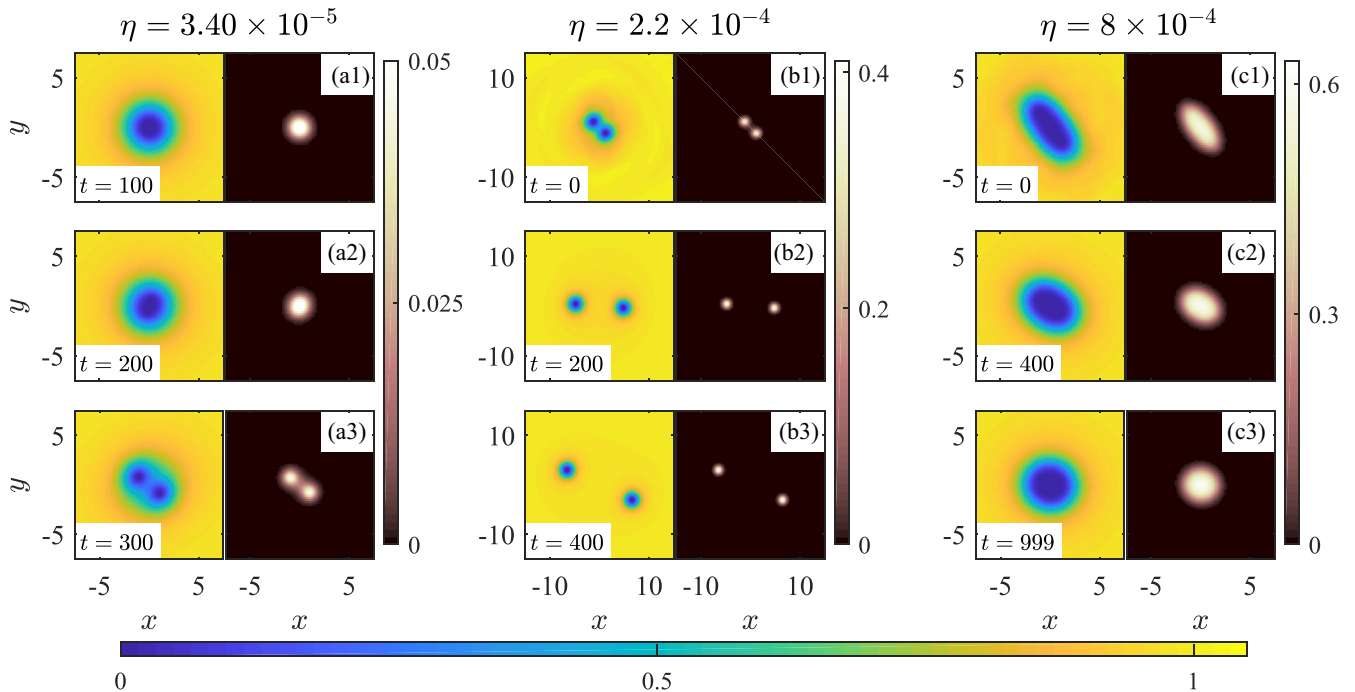


FIG. 10. Vortex pair dynamics with damping for various η . In panels (a1)–(a3), atoms of the second species stay confined to the SQV vortex cores when the MQV decays. In panels (b1)–(b3) the vortices spiral out in an η independent manner, with the species 2 atoms tracking the motion of the vortex cores. In panels (c1)–(c3), η is above the critical fraction, hence the system lowers its energy by recombining into a single, central MQV.

In accordance with this expectation, the dynamics observed for $t > 300$ at $\eta = 3.4 \times 10^{-5}$ [i.e., after the last frame shown in panel (a)] also follow the point-vortex behavior. From this, we conclude that the modified dynamics in two component condensates is absent when species 2 atoms are split into distinct parcels which occupy the separate vortex cores. In other words, the stabilization is a feature of a single parcel of species 2 atoms shared across the vortices.

To support this conclusion, in panels (c1)–(c3) we take such a configuration as our initial condition. The corresponding vortex mode at this η value has positive energy, hence the separation of vortices (while retaining a single parcel of species 2 atoms) is associated with an energy gain relative to the stationary MQV. As the system evolves, the vortices orbit in the clockwise sense and damping reduces the vortex separation to lower the energy of the system. At late times, we recover a stationary, central MQV. This demonstrates that MQVs seeded with species 2 atoms above a critical fraction can be inherently stable objects even when a dissipation mechanism is present.

V. DISCUSSION

The results presented here show that, in a two-component condensate confined in a bucket trap in the immiscible regime, multiply quantized vortices (MQVs) in the first component can be stabilized when a relatively small number of atoms of the second component collect in the vortex core. We have found that if the fraction η of atoms of the second component is small, the growth rate of the dynamically unstable mode which causes vortex splitting is smaller than when the second component is absent. We found that there exists a critical

fraction η_c above which vortex decay is energetically unfavorable. Hence, for $\eta > \eta_c$, MQVs are stabilized even in the presence of a dissipation mechanism since it would cost energy to separate them. A consequence of the stabilization mechanism is that nearby corotating vortices can orbit in the opposite sense to their individual rotations when enough atoms of the second component are shared across the cores.

The parameters that we have used in this model were chosen such that an experiment would be reasonably feasible. The greatest challenge in performing this experiment would be creating a trapping potential profile that directly matches what we have used here; however, since the first realization of a uniform trapping potential [37], advancements have been made in generating homogeneous condensates [38,39], with traps of the size of $\approx 100 \mu\text{m}$. We also expect this phenomenon to persist in harmonic traps since the instability is a feature of the vortex core rather than the details of the trapping potential (see, e.g., [10] for an example where the normal mode spectra of MQVs in harmonic and boxlike trapping potentials are qualitatively the same in one-component condensates).

Our results stand in contrast to those in [40], where a miscible, two-component condensate (with equal mass and self-interaction parameters) was shown to be more unstable than vortices in one-component condensates. This is a result of the region where spin waves have negative energy density extending outside the vortex core. It is an interesting parallel then that in the opposite case, where the mixtures are immiscible, MQVs can be made more or completely stable. We comment that our findings in Fig. 2 are also reminiscent of excitations of coreless vortices in spinor BECs; see, e.g., [41]. There, one of the spin sublevels (containing no vortex) fills the core of an $\ell = 2$ vortex in one of the other sublevels. This

system also contains a vortex mode that can cause a dynamical instability, and increasing the total magnetization (analogous to our parameter η) is seen to suppress the dynamical instability by reducing the magnitude of vortex mode energy. An important difference is that in our case, there is a critical η value where the vortex mode energy changes sign (implying its excitation does not lower the energy of the system), which does not happen in [41].

Our results further demonstrate that even in dynamic scenarios, the atoms of the second component remain attached to the vortex cores rather than becoming scattered about the trap. Therefore, the proposed method of MQV stabilization could provide a solution to the problem of destructive imaging, as suggested in [42]. The most common method to image a condensate is absorption imaging, which consists of illuminating the cold gas with a laser and measuring the shadow cast by absorption [43]. Although this method provides a detailed image of the condensate, irradiating the system drastically changes its energy and dynamics, and in the worst case destroys the condensate [44]. It is also possible to remove a small fraction of the atoms of a specific component of a condensate from a trap and to image them independently [45]. If one stabilized vortex cores with a second component, the use of a specific microwave pulse could outcouple only secondary component atoms, resulting in an image describing vortex core locations without affecting the dynamics of the primary component. As this stabilization has proven robust, vortex cores undergoing rapid motion could be reliably imaged and tracked.

An added consequence of the stabilization is that MQVs (and also SQVs) are endowed with an extra degree of freedom relative to one-component condensates where an excited vortex can only radiate sound. Here, the extra degree of freedom is the excitations of the second component, which would allow for more complicated interactions in systems containing more than one vortex. This situation has some analogy with superfluid ^3He , where vortices may have a double vortex core whose rotational symmetry about the vortex axis is broken [46]. By creating a natural ribbon, the double vortex structure would help the definition of superfluid helicity [47].

Another interesting question relates to the dynamics of vortices in 3D condensates. If atoms of the second component are unevenly distributed along a pair of nearby vortex filaments, different segments of the vortex filament could feasibly orbit in opposite directions. This may induce vortex reconnections, with potential consequences for superfluid turbulence in two-component mixtures. We note that a similar system was studied in [48] where the second species was made to flow along the vortex core of the primary condensate.

A further possibility we raise involves the nucleation of vortices containing atoms of the second component. In a system of species 1 atoms in which vortices are absent, a small amount of species 2 could be added close to the edge of the trapping potential where the density drops to zero. Rotating the condensate would lead to vortex nucleation close to the edge of the trap, and it is feasible such vortices would carry atoms of the second species. Furthermore, as we have seen, for large enough proportions of atoms in species 2, MQVs can be energetically preferable to SQVs, raising the intriguing possibility of nucleating vortices with large winding numbers. To achieve this, the effect of dissipation on species 2 atoms would

need to be much smaller than on species 1 atoms, otherwise the former would dissipate out of the system. In that case, one could imagine creating a lattice of MQVs on timescales before dissipation of the second species became significant.

Finally, since the vortex mode has vanishing oscillation frequency at the critical fraction η_c , it would be interesting to investigate the nonlinear dynamics in the vicinity of this value to see if static (i.e., nonorbiting) configurations of vortices can be constructed.

ACKNOWLEDGMENTS

We thank Tom Billam and Connor F. Swales for involvement in the early stages of this work. We are also grateful to Andrea Richaud and the anonymous referee for helpful comments. For the purpose of open access, the author has applied a Creative Commons Attribution (CC BY) licence to any Author Accepted Manuscript version arising. This work was supported in part by the STFC Quantum Technology Grants No. ST/T005858/1 (S.P. and R.G.), No. ST/T006900/1 (C.F.B.), and King's College London (A.G.). R.G. also acknowledges support from the Perimeter Institute. Research at Perimeter Institute is supported by the Government of Canada through the Department of Innovation, Science and Economic Development Canada and by the Province of Ontario through the Ministry of Research, Innovation and Science.

APPENDIX A: DIMENSIONAL REDUCTION

The action for the two-component system in three-dimensional (3D) space is

$$S^{3D} = \int dt d^2\mathbf{x} \left[\sum_j (i\hbar\Psi_j^{3D*}\dot{\Psi}_j^{3D} - \mathcal{H}_j^{3D}) - \mathcal{H}_I^{3D} \right],$$

with

$$\mathcal{H}_j^{3D} = \Psi_j^{3D*} [\hat{K}_j^{3D} + V_j^{3D}(\mathbf{x}) - \tilde{\mu}_j^{3D}] \Psi_j^{3D} + \frac{G_j^{3D}}{2} |\Psi_j^{3D}|^4,$$

$$\mathcal{H}_I = G_{12}^{3D} |\Psi_1^{3D}|^2 |\Psi_2^{3D}|^2.$$

We now assume a tight confinement in the vertical (z) direction and seek an action governing the dimensionally reduced dynamics in the (x, y) plane. To this end, we write

$$V_j^{3D}(x, y, z) = V(x, y) + \frac{1}{2} M_j \omega_j^2 z^2, \quad \tilde{\mu}_j^{3D} = \tilde{\mu}_j + \frac{\hbar\omega_j}{2},$$

where $V(x, y)$ and $\tilde{\mu}_j$ are the 2D bucket trap and chemical potentials in the main text, and the z -dependent piece of V_j^{3D} is a harmonic trap of frequency ω_j . The breakdown of the chemical potential in this way amounts to assuming that the z -dependent piece of the wave function is the ground state if we also assume $\tilde{\mu}_j \ll \hbar\omega_j$ and $\Psi_j^{3D}(x, y, z, t) = \Psi_j^{2D}(x, y, t) f_j(z)$. The 3D action can then be split as $S^{3D} = S_z + S$, where $S_z \sim O(\hbar\omega_j)$ and $S \sim O(\tilde{\mu}_j)$. The vertical part is

$$S_z = \int dt d^2\mathbf{x} |\Psi_j^{2D}|^2 \int dz \sum_j \times \left(\frac{\hbar\omega_j}{2} |f_j|^2 - \frac{\hbar^2}{2M_j} |\partial_z f_j|^2 - \frac{1}{2} M_j \omega_j^2 z^2 |f_j|^2 \right),$$

whose variation yields

$$\frac{\hbar^2}{2M_j} \partial_z^2 f_j + \left(\frac{\hbar\omega_j}{2} - \frac{1}{2} M_j \omega_j^2 z^2 \right) f_j = 0, \quad (\text{A1})$$

which has solutions

$$f_j(z) = e^{-z^2/2d_j^2}, \quad d_j^2 = \frac{\hbar}{M_j \omega_j}. \quad (\text{A2})$$

The f_j can then be inserted into the 2D action and the z integrals evaluated. Terms involving $|\Psi_j^{2D}|^2$ (including the derivative term), $|\Psi_j^{2D}|^4$, and $|\Psi_1^{2D} \Psi_2^{2D}|^2$ are proportional to the following z integrals:

$$\int dz f_j^2 = d_j \sqrt{\pi}, \quad \int dz f_j^4 = d_j \sqrt{\pi/2}, \quad (\text{A3})$$

and

$$\int dz f_1^2 f_2^2 = d_{12} \sqrt{\pi}, \quad d_{12}^{-2} = d_1^{-2} + d_2^{-2}. \quad (\text{A4})$$

Finally, we obtain the action in (5) once we make the identifications

$$\Psi_j = (d_j \sqrt{\pi})^{\frac{1}{2}} \Psi_j^{2D} \quad (\text{A5})$$

and

$$G_j = \frac{G_j^{3D}}{\sqrt{2\pi} d_j}, \quad G_{12} = \frac{d_{12} G_{12}^{3D}}{\sqrt{\pi} d_1 d_2}. \quad (\text{A6})$$

The interaction parameters are related to the scattering lengths a_j through [35]

$$G_j^{3D} = \frac{4\pi \hbar^2 a_j}{M_j}, \quad G_{12}^{3D} = \frac{2\pi \hbar^2 a_{12}}{M_{12}}, \quad (\text{A7})$$

where $M_{12} = M_1 M_2 / (M_1 + M_2)$ is the reduced mass of the two species. The dimensionless parameters defined in Sec. II C become

$$g_2 = \frac{d_1 M_1 a_2}{d_2 M_2 a_1}, \quad g_{12} = \frac{d_{12} M_1 a_{12}}{\sqrt{2} d_2 M_{12} a_1}, \quad (\text{A8})$$

or in terms of the harmonic trapping frequencies,

$$g_2 = \sqrt{\frac{M_1 \omega_2}{M_2 \omega_1}} \frac{a_2}{a_1}, \quad g_{12} = \frac{1 + M_1/M_2}{\sqrt{1 + \frac{M_1 \omega_1}{M_2 \omega_2}}} \frac{a_{12}}{\sqrt{2} a_1}. \quad (\text{A9})$$

The vertical confinement applied to the two species is the same provided $M_1 \omega_1^2 = M_2 \omega_2^2$. In this case, we find

$$g_2 = \left(\frac{M_1}{M_2} \right)^{3/4} \frac{a_2}{a_1}, \quad g_{12} = \frac{1 + M_1/M_2}{\sqrt{1 + (M_1/M_2)^{1/2}}} \frac{a_{12}}{\sqrt{2} a_1}.$$

The s -wave scattering lengths for the ^{87}Rb and ^{133}Cs mixture are $a_1 = 100a_0$, $a_2 = 280a_0$, and $a_{12} = 650a_0$ [26], where a_0 is the Bohr radius [35]. Using $M_1/M_2 = 87/133$, we obtain the values

$$g_2 = 2.04, \quad g_{12} = 5.65, \quad (\text{A10})$$

which are the values quoted in the main text.

APPENDIX B: BOUNDARY CONDITIONS

As $r \rightarrow 0$, we have $n_1 \rightarrow 0$ and $\varepsilon \rightarrow 0$. The fields u_1 and v_1 each obey the Schrödinger equation, whose regular solutions are of the form

$$u_1 \sim J_{m+\ell}(\alpha_+ r), \quad v_1 \sim J_{m-\ell}(\alpha_- r), \quad (\text{B1})$$

with $\alpha_{\pm}^2 = 2(1 - g_{12} n_2 \pm \omega)$. Thus, the boundary conditions are

$$\begin{aligned} m = \ell : \quad & u_1(r=0) = \partial_r v_1|_{r=0} = 0, \\ m = -\ell : \quad & \partial_r u_1|_{r=0} = v_1(r=0) = 0, \\ |m| \neq \ell : \quad & u_1(r=0) = v_1(r=0) = 0. \end{aligned} \quad (\text{B2})$$

The fields u_2 and v_2 remained coupled to one another, although they do decouple from u_1 and v_1 . To find their asymptotic form, we can expand in power series about $r = 0$ and apply the method of Frobenius. Writing

$$u_2 = \sum_{n=0}^{\infty} b_n^+ r^{n+p^+}, \quad v_2 = \sum_{n=0}^{\infty} b_n^- r^{n+p^-}, \quad (\text{B3})$$

the equations of motion become

$$\begin{aligned} & \sum_{n=0}^{\infty} [(n+p^+)^2 - m^2] b_n^+ r^{n+p^+} \\ & + \sum_{n=2}^{\infty} [\beta^+ b_{n-2}^+ - 2g_2 n_2 b_{n-2}^-] r^{n+p^+} = 0, \\ & \sum_{n=0}^{\infty} [(n+p^-)^2 - m^2] b_n^- r^{n+p^-} \\ & + \sum_{n=2}^{\infty} [\beta^- b_{n-2}^- - 2g_2 n_2 b_{n-2}^+] r^{n+p^-} = 0, \end{aligned} \quad (\text{B4})$$

with $\beta^{\pm} = 2(\mu_2 - 2g_2 n_2 \pm \omega)$. The first term in the series yields the values of p^{\pm} . The regular solutions are each given by $p^{\pm} = |m|$. Hence the asymptotics at the origin are $u_2 \sim r^{|m|}$ and $v_2 \sim r^{|m|}$ leading to the boundary conditions

$$\begin{aligned} m = 0 : \quad & \partial_r u_2|_{r=0} = \partial_r v_2|_{r=0} = 0, \\ m \neq 0 : \quad & u_2(r=0) = v_2(r=0) = 0. \end{aligned} \quad (\text{B5})$$

APPENDIX C: RESOLUTION

From the procedure outlined in Sec. II D, we obtain the chemical potentials $\mu_j^0 = \mu_j + \Delta\mu_j$, where μ_j is the true value that one would obtain in the continuum limit. By checking for a range of resolutions, we observe that the error $\Delta\mu_j$ scales linearly with $\varepsilon_r = \Delta\tau$ and $\varepsilon_r = \Delta r^2$. This error will offset the normal mode frequencies calculated in Fig. 2, and therefore the value of η_c obtained from looking where the vortex mode has zero frequency.

We account for this offset using the following linear perturbation theory argument. We start with the resolution used to produce Fig. 2, $\varepsilon_r^0 = 4 \times 10^{-4}$ and $\varepsilon_r^0 = (45/800)^2$, and we expand the vortex mode frequency in the vicinity of the zero

crossing,

$$\omega = \omega^0 + \partial_\eta \omega^0 (\eta - \eta_c^0), \quad (\text{C1})$$

where η_c^0 is our prediction for the critical η value at this resolution and $\omega^0 = 0$ by definition. The gradient $\partial_\eta \omega^0$ is measured from Fig. 2. Now consider a change in the resolution. The expansion above to leading order becomes

$$\omega = \omega^0 + \delta\omega + \partial_\eta \omega^0 (\eta - \eta_c^0), \quad (\text{C2})$$

where $\delta\omega$ is the shift in the value of ω at η_c^0 . Solving $\omega = 0$ gives the new value of η_c ,

$$\eta_c = \eta_c^0 - \frac{\delta\omega}{\partial_\eta \omega^0}. \quad (\text{C3})$$

Now, to compute η_c at infinite resolution, we need to estimate $\delta\omega$ as we take ϵ_τ and ϵ_r to zero. To do this, we use the fact that ω depends linearly on ϵ_τ and ϵ_r , and we expand the value of ω at η_c^0 ,

$$\omega(\eta_c^0) = \omega_\tau^0 (\epsilon_\tau - \epsilon_\tau^0) + \omega_r^0 (\epsilon_r - \epsilon_r^0), \quad (\text{C4})$$

with

$$\omega_\tau^0 \equiv \left. \frac{\partial \omega}{\partial \epsilon_\tau} \right|_{\epsilon_r^0, \epsilon_\tau^0}, \quad \omega_r^0 \equiv \left. \frac{\partial \omega}{\partial \epsilon_r} \right|_{\epsilon_r^0, \epsilon_\tau^0}. \quad (\text{C5})$$

We can estimate these gradient terms by independently varying the resolutions away slightly from their initial values. Once ω_r^0 and ω_τ^0 are known, the frequency shift at infinite resolution is given by

$$\delta\omega = -\omega_\tau^0 \epsilon_\tau^0 - \omega_r^0 \epsilon_r^0. \quad (\text{C6})$$

The expression for η_c in the continuum limit is therefore

$$\eta_c = \eta_c^0 + \frac{\omega_\tau^0 \epsilon_\tau^0 + \omega_r^0 \epsilon_r^0}{\partial_\eta \omega^0}. \quad (\text{C7})$$

Using $\eta_c^0 = 5.933 \times 10^{-4}$, we estimate the true value to be $\eta_c = 5.936 \times 10^{-4}$.

When performing the nonlinear simulations of Sec. IV, it was not computationally feasible to use the same resolution used for Fig. 2. In Fig. 11, we compare the spectrum for $\Delta\tau = 4 \times 10^{-4}$ and 800 radial points (red curves) with the same for $\Delta\tau = 5 \times 10^{-3}$ and 256 radial points (black lines). Bulk excitations (horizontal lines) are insensitive to the change since they occupy a region where there are a large number of grid points. The main difference is in the vortex mode frequency, since this mode is covered by far fewer grid points at lower resolution. This leads to a slight displacement of the instability bubbles in the plot of $\text{Im}[\omega]$. We also show with black dots the values of $\text{Re}[\omega]$ and $\text{Im}[\omega]$ extracted from the full numerics, namely Fig. 8. We observe good agreement for all η values, although the largest η point is displaced slightly above its true value on the plot of $\text{Im}[\omega]$. We interpret this as being due to finite-size effects similar to those studied in [11], which onset earlier for this particular mode and make it more difficult to extract the growth rate.

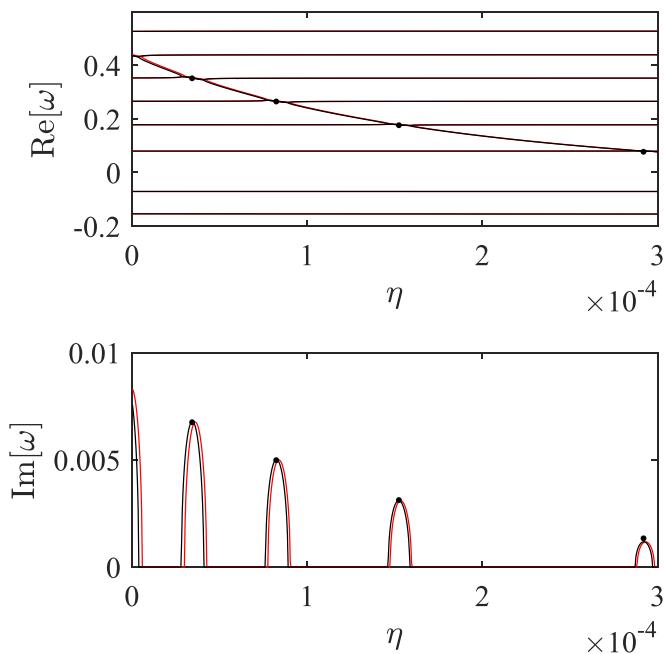


FIG. 11. Normal-mode spectra for resolutions $\Delta\tau = 4 \times 10^{-4}$ and 800 radial points (red) used in Fig. 2, and $\Delta\tau = 5 \times 10^{-3}$ and 256 radial points (black) comparable to that used in Sec. IV.

APPENDIX D: SMALL r INTEGRAL

Here we evaluate the phase integral inside the vortex core in the small r approximation. The integral is

$$I = \int_{r_-}^{r_+} \sqrt{-W_+} dr. \quad (\text{D1})$$

For $W_+(0) > 0$, r_\pm are the smallest r values for which $W_+ = 0$, while for $W_+(0) < 0$, $r_- = 0$ and r_+ is the smallest r value for which $W_+ = 0$. Close to the axis, we can expand W_+ treating r as small,

$$W_+ = \frac{(m - \ell)^2}{r^2} - 2(1 - g_{12}n_{2,0} - \omega) + g_{12}n_{2,0}''r^2 + (4n_{1,0}'''' + 2n_{2,0}''''r^4/4! + O(r^6)), \quad (\text{D2})$$

where we have expanded $n_{1,2}$ up to and including quartic order terms. Since the small r behavior of component 1 is $n_1 \sim r^{2\ell}$, we assume at this stage that we have an $\ell = 2$ vortex so that $n_{0,1}'''' \neq 0$. To perform the calculation for $\ell \neq 2$, one would need to retain larger terms in the r expansion. The unstable mode for the doubly quantized vortex occurs for $m = \ell = 2$, hence we can write W_+ in the form

$$W_+ = 2\omega - 2U - \alpha r^2 + \beta r^4, \quad U = 1 - g_{12}n_{2,0}, \\ \alpha = -g_{12}n_{2,0}'', \quad \beta = (4n_{1,0}'''' + 2n_{2,0}''''r^4/4!), \quad (\text{D3})$$

where α and β are positive constants. For small enough η , the minimum of W_+ will be located in the region where this expansion is valid. The minimum is $r_0 = \sqrt{\alpha/2\beta}$ and the value of the potential there is $W_0 = 2(\omega - \omega_0)$, where $\omega_0 = U + \alpha^2/8\beta$ is the maximum frequency which propagates in the cavity and is positive for small η . Now we evaluate the cavity integral for ω close to ω_0 . For this we expand W_+ this

time around r_0 ,

$$W_+ = W_0 + 2\alpha(r - r_0)^2. \quad (\text{D4})$$

In this approximation, $r_{\pm} = r_0 \pm \sqrt{-W_0/2\alpha}$. We can then compute I ,

$$\begin{aligned} I &= \int_{r_-}^{r_+} dr \sqrt{-W_0 - 2\alpha(r - r_0)^2}, \\ &= \frac{-W_0}{\sqrt{2\alpha}} \int_{-1}^1 dz \sqrt{1 - z^2} = -\frac{\pi W_0}{2\sqrt{2\alpha}}, \end{aligned} \quad (\text{D5})$$

which can be written as

$$I(\omega) = \frac{\pi(\omega_0 - \omega)}{|2g_{12}n_{2,0}'|^{1/2}} + O[(\omega_0 - \omega)^2], \quad (\text{D6})$$

as stated in (32) of the main text. It is also instructive to write ω_0 as

$$\omega_0 = 1 - g_{12}(n_{0,2} + n_{0,2}'^2/4), \quad (\text{D7})$$

where the term in parentheses is slightly smaller than the value of n_2 at r_0 . Since n_2 increases with η , we deduce that ω_0 decreases as η is increased from 0.

-
- [1] C. F. Barenghi and N. G. Parker, *A Primer on Quantum Fluids* (Springer, Berlin, 2016).
- [2] S. K. Adhikari, Stable controllable giant vortex in a trapped Bose-Einstein condensate, *Laser Phys. Lett.* **16**, 085501 (2019).
- [3] S. K. Adhikari and P. Muruganandam, Effect of an impulsive force on vortices in a rotating Bose-Einstein condensate, *Phys. Lett. A* **301**, 333 (2002).
- [4] R. Srinivasan, Vortices in Bose-Einstein condensates: A review of the experimental results, *Pramana* **66**, 3 (2006).
- [5] P. Kuopanportti, N. V. Orlova, and M. V. Milošević, Ground-state multiquantum vortices in rotating two-species superfluids, *Phys. Rev. A* **91**, 043605 (2015).
- [6] H. Pu, C. K. Law, J. H. Eberly, and N. P. Bigelow, Coherent disintegration and stability of vortices in trapped Bose condensates, *Phys. Rev. A* **59**, 1533 (1999).
- [7] Y. Kawaguchi and T. Ohmi, Splitting instability of a multiply charged vortex in a Bose-Einstein condensate, *Phys. Rev. A* **70**, 043610 (2004).
- [8] Y. Shin, M. Saba, M. Vengalattore, T. A. Pasquini, C. Sanner, A. E. Leanhardt, M. Prentiss, D. E. Pritchard, and W. Ketterle, Dynamical Instability of a Doubly Quantized Vortex in a Bose-Einstein Condensate, *Phys. Rev. Lett.* **93**, 160406 (2004).
- [9] T. Ioshima, M. Okano, H. Yasuda, K. Kasa, J. A. M. Huhtamäki, M. Kumakura, and Y. Takahashi, Spontaneous Splitting of a Quadruply Charged Vortex, *Phys. Rev. Lett.* **99**, 200403 (2007).
- [10] L. Giacomelli and I. Carusotto, Ergoregion instabilities in rotating two-dimensional Bose-Einstein condensates: Perspectives on the stability of quantized vortices, *Phys. Rev. Res.* **2**, 033139 (2020).
- [11] S. Patrick, A. Geelmuyden, S. Erne, C. F. Barenghi, and S. Weinfurter, Origin and evolution of the multiply quantized vortex instability, *Phys. Rev. Res.* **4**, 043104 (2022).
- [12] S. Patrick, A. Geelmuyden, S. Erne, C. F. Barenghi, and S. Weinfurter, Quantum vortex instability and black hole super-radiance, *Phys. Rev. Res.* **4**, 033117 (2022).
- [13] J. Qin, G. Dong, and B. A. Malomed, Stable giant vortex annuli in microwave-coupled atomic condensates, *Phys. Rev. A* **94**, 053611 (2016).
- [14] C. J. Myatt, E. A. Burt, R. W. Ghrist, E. A. Cornell, and C. E. Wieman, Production of Two Overlapping Bose-Einstein Condensates by Sympathetic Cooling, *Phys. Rev. Lett.* **78**, 586 (1997).
- [15] D. S. Hall, M. R. Matthews, J. R. Ensher, C. E. Wieman, and E. A. Cornell, Dynamics of Component Separation in a Binary Mixture of Bose-Einstein Condensates, *Phys. Rev. Lett.* **81**, 1539 (1998).
- [16] D. J. McCarron, H. W. Cho, D. L. Jenkin, M. P. Köppinger, and S. L. Cornish, Dual-species bose-einstein condensate of ^{87}Rb and ^{133}Cs , *Phys. Rev. A* **84**, 011603(R) (2011).
- [17] S. B. Papp, J. M. Pino, and C. E. Wieman, Tunable Miscibility in a Dual-Species Bose-Einstein Condensate, *Phys. Rev. Lett.* **101**, 040402 (2008).
- [18] J. Kronjäger, C. Becker, M. Brinkmann, R. Walser, P. Navez, K. Bongs, and K. Sengstock, Evolution of a spinor condensate: Coherent dynamics, dephasing, and revivals, *Phys. Rev. A* **72**, 063619 (2005).
- [19] S. Tojo, Y. Taguchi, Y. Masuyama, T. Hayashi, H. Saito, and T. Hirano, Controlling phase separation of binary Bose-Einstein condensates via mixed-spin-channel Feshbach resonance, *Phys. Rev. A* **82**, 033609 (2010).
- [20] P. Kuopanportti, S. Bandyopadhyay, A. Roy, and D. Angom, Splitting of singly and doubly quantized composite vortices in two-component Bose-Einstein condensates, *Phys. Rev. A* **100**, 033615 (2019).
- [21] P. Mason, Solid-body rotation and giant circulations in coupled condensates, *J. Phys. B* **50**, 165002 (2017).
- [22] X. Zhang, L. Wen, C. Dai, R. Dong, H. Jiang, H. Chang, and S. Zhang, Exotic vortex lattices in a rotating binary dipolar Bose-Einstein condensate, *Sci. Rep.* **6**, 19380 (2016).
- [23] B. Dong, L. Wang, G. Chen, W. Han, S. Zhang, and X. Zhang, Equilibrium vortex lattices of a binary rotating atomic Bose-Einstein condensate with unequal atomic masses, *Ann. Phys.* **373**, 178 (2016).
- [24] X. Ma, R. Driben, B. A. Malomed, T. Meier, and S. Schumacher, Two-dimensional symbiotic solitons and vortices in binary condensates with attractive cross-species interaction, *Sci. Rep.* **6**, 34847 (2016).
- [25] P. Ao and S. T. Chui, Binary Bose-Einstein condensate mixtures in weakly and strongly segregated phases, *Phys. Rev. A* **58**, 4836 (1998).
- [26] T. L. Ho and V. B. Shenoy, Binary Mixtures of Bose Condensates of Alkali Atoms, *Phys. Rev. Lett.* **77**, 3276 (1996).
- [27] E. Timmermans, Phase Separation of Bose-Einstein Condensates, *Phys. Rev. Lett.* **81**, 5718 (1998).
- [28] C. Wang, C. Gao, C. M. Jian, and H. Zhai, Spin-Orbit Coupled Spinor Bose-Einstein Condensates, *Phys. Rev. Lett.* **105**, 160403 (2010).

- [29] C. Wu, I. Mondragon-Shem, and X. Zhou, Unconventional Bose-Einstein condensations from spin-orbit coupling, *Chin. Phys. Lett.* **28**, 097102 (2011).
- [30] A. Richaud, V. Penna, R. Mayol, and M. Guilleumas, Vortices with massive cores in a binary mixture of Bose-Einstein condensates, *Phys. Rev. A* **101**, 013630 (2020).
- [31] A. Richaud, V. Penna, and A. L. Fetter, Dynamics of massive point vortices in a binary mixture of Bose-Einstein condensates, *Phys. Rev. A* **103**, 023311 (2021).
- [32] V. P. Ruban, Direct and reverse precession of a massive vortex in a binary Bose-Einstein condensate, *JETP Lett.* **115**, 415 (2022).
- [33] A. Richaud, P. Massignan, V. Penna, and A. L. Fetter, Dynamics of a massive superfluid vortex in r^k confining potentials, *Phys. Rev. A* **106**, 063307 (2022).
- [34] A. Richaud, G. Lamporesi, M. Capone, and A. Recati, Mass-driven vortex collisions in flat superfluids, *Phys. Rev. A* **107**, 053317 (2023).
- [35] R. W. Pattinson, T. P. Billam, S. A. Gardiner, D. J. McCarron, H. W. Cho, S. L. Cornish, N. G. Parker, and N. P. Proukakis, Equilibrium solutions for immiscible two-species Bose-Einstein condensates in perturbed harmonic traps, *Phys. Rev. A* **87**, 013625 (2013).
- [36] Note that the n_m are equivalent for small amplitudes to the $\delta n_{j,m}$ defined (20) in the case of a single component. However, (20) are strictly modes of the linear theory while n_m are Fourier components of the full nonlinear field, which differ from the linear prediction when the amplitude is large.
- [37] N. Navon, A. L. Gaunt, R. P. Smith, and Z. Hadzibabic, Emergence of a turbulent cascade in a quantum gas, *Nature (London)* **539**, 72 (2016).
- [38] S. P. Johnstone, A. J. Groszek, P. T. Starkey, C. J. Billington, T. P. Simula, and K. Helmerson, Evolution of large-scale flow from turbulence in a two-dimensional superfluid, *Science* **364**, 1267 (2019).
- [39] G. Gauthier, M. T. Reeves, X. Yu, A. S. Bradley, M. A. Baker, T. A. Bell, H. Rubinsztein-Dunlop, M. J. Davis, and T. W. Neely, Giant vortex clusters in a two-dimensional quantum fluid, *Science* **364**, 1264 (2019).
- [40] A. Berti, L. Giacomelli, and I. Carusotto, Superradiant phononic emission from the analog spin ergoregion in a two-component Bose-Einstein condensate, [arXiv:2212.07337](https://arxiv.org/abs/2212.07337).
- [41] M. Takahashi, V. Pietilä, M. Möttönen, T. Mizushima, and K. Machida, Vortex-splitting and phase-separating instabilities of coreless vortices in $F = 1$ spinor Bose-Einstein condensates, *Phys. Rev. A* **79**, 023618 (2009).
- [42] R. Doran, A. W. Baggaley, and N. G. Parker, Vortex solutions in a binary immiscible Bose-Einstein condensate, [arXiv:2207.12913](https://arxiv.org/abs/2207.12913).
- [43] B. P. Anderson and M. A. Kasevich, Spatial observation of Bose-Einstein condensation of ^{87}Rb in a confining potential, *Phys. Rev. A* **59**, R938 (1999).
- [44] T. Pyragius, Developing and building an absorption imaging system for ultracold atoms, [arXiv:1209.3408](https://arxiv.org/abs/1209.3408).
- [45] S. Serafini, M. Barbiero, M. Debortoli, S. Donadello, F. Larcher, F. Dalfovo, G. Lamporesi, and G. Ferrari, Dynamics and Interaction of Vortex Lines in an Elongated Bose-Einstein Condensate, *Phys. Rev. Lett.* **115**, 170402 (2015).
- [46] E. V. Thuneberg, Identification of Vortices in Superfluid $^3\text{He-B}$, *Phys. Rev. Lett.* **56**, 359 (1986).
- [47] H. Salman, Helicity conservation and twisted Seifert surfaces for superfluid vortices, *Proc. R. Soc. A* **473**, 20160853 (2017).
- [48] S. Hayashi, M. Tsubota, H. Takeuchi, Instability crossover of helical shear flow in segregated Bose-Einstein Condensates, *Phys. Rev. A* **87**, 063628 (2013).